Stress and Deformation of Thin Films and Patterned Lines on Substrates

by

Tae-Soon Park

Submitted to the Department of Materials Science and Engineering
in partial fulfillment of the requirements for the degree of

Doctor of Philosophy in Electronic Materials

at the

MASSACHUSETTS INSTITUTE OF TECHNOLOGY

June 2002

Author .....
Department of Materials Science and Engineering
May. 10, 2002

Certified by .....
Subra Suresh
R. P. Simmons Professor of Materials Science and Engineering
Thesis Supervisor

Accepted by .....
Harry L. Tuller
Professor of Ceramics and Electronic Materials
Chair, Departmental Committee on Graduate Students

Stress and Deformation of Thin Films and Patterned Lines on Substrates

by

Tae-Soon Park

Submitted to the Department of Materials Science and Engineering
on May. 10, 2002, in partial fulfillment of the
requirements for the degree of
Doctor of Philosophy in Electronic Materials

Abstract

The thermomechanical response of thin films/lines on thicker substrates under internal loadings resulting from material mismatch is examined. As the well-known Stoney formula is limited to isotropic, blanket films that undergo only small deformations, proper interpretation of curvature-stress relationships for new film geometries and for new experimental testing techniques requires an extension of this analytical framework. Mismatch stresses in thin films/lines and consequent curvature evolution of the film/line-substrate system are investigated in realistic, complex geometries relevant to industrial trends, such as high line aspect ratio, multi-level structure, and large diameter wafers. A combined analytical and numerical method is presented to evaluate curvature and stress evolution in metal and dielectric lines in an interconnect structure on a Si substrate during fabrication steps and subsequent thermal loading. An engineering map based on a closed-form solution for volume-averaged thermal stresses in lines is developed for material selection and design optimization. Coherent gradient sensing (CGS), an optical, full-field and vibration-insensitive experimental method, is used to study large deformation behavior of thin film-substrate systems by measuring the gradient of out-of-plane displacement of deformed surfaces. Experimental results are discussed in terms of the limitation of the small deformation theory upon which the Stoney formula is predicated. In particular, this work seeks to incorporate anisotropy and non-linearity arising from geometrical changes such as directional patterning and large deformation in the range of isotropic and linear-elastic material behavior.

Thesis Supervisor: Subra Suresh
Title: R. P. Simmons Professor of Materials Science and Engineering

Acknowledgments

Time is coming again to complete another chapter in my life. During last five years I owe a lot to people around me to meet a challenge I could not face without them. The smallest thing I can do for now is to express my gratitude here, even if it is monologue, for keeping them in my mind. First of all I would like to thank my advisor, Prof. Subra Suresh, for providing me great opportunity and supporting me through my stay at MIT. Since I met him for the first time, when I was desperate for research assistant position under economic crisis in my home country, he has always been showing me the way I can deal with problems. I would also like to express my gratitude to my committee members, Prof. Carl V. Thompson and Prof. S. Mark Spearing, for valuable comments and encouragement. I really enjoyed my internship at Intel Corporation during summer, 2000, thanks to help from Dr. Sadasivan Shankar and Dr. Daniel Pantuso, and also got great help from Prof. Ares. J. Rosakis and Dr. David Owen during my visit at California Institute of Technology.

I feel I am lucky because I am one of LEXCOM members. First I thank Mr. George Labonte and Mr. Kenneth Greene for helping me out everything from the beginning. When I joined LEXCOM in January, 1998, old fellows -Venkatesh, Raj, Olivera, Fred, and Andrew :)- tried to make me feel at home in the basement. I also thank Krystyn and Tim for reading everything in my thesis, Brett and John for smiling at me everytime, then Kob for staying till late every night. Yoonjoon did not say much, but I could hear much from him. I really enjoyed staying with him for a long time. I appreciate help on computation from Ming and hope Ruth and Benedict will enjoy their stay in LEXCOM. I am also happy to have spent time with Prof. Chong-Su Lee, Dr. Hyang-Jin Koh, Dr. Jae-Joong Kim and Dr. Yong-Nam Kwon all from POSTECH. I will miss that time when we could chat in Korean over lunch time.

In a shaky beginning at MIT, my former advisor, Prof. Euijoon Yoon, helped me a lot on choice of thesis advisor and research topic. I'm thankful to Sanghoon Ahn

and Minha Hwang for settling me down during my first year. I also enjoyed staying with Hyung-Soo Moon and Jekwan Ryu during my second year. I have to say I am indebted to Nami Cho for her careful understanding in a tough time, and sorry that there is no way to repay her except for wishing the happiest life. I would like to keep my memory with my wonderful classmates- Yongki Min, Jinwook Lee and Jin-Woo Park - who got through preparation for qualifying exam together and with supportive friends- Dongwon Choi, Heejae Kim and Jeeyoung Choi - for not letting me alone.

Finally I have to confess that I do love my family- my sister, Ji-Young, and my parents. Even though we are separate physically now, my heart is always with you and I promise to you that I will keep going till we get together again. I am looking forward to seeing what my next chapter looks like...

Contents

List of Figures

List of Tables

Chapter 1

Introduction

Thin films on much thicker substrates have been used in a wide range of engineering applications, including ceramic films on turbo-engine structures (a mm-thick film on a cm-thick substrate) for thermal barrier coatings (TBC) and compound semiconductor thin films on InP substrates (a nm-thick film on a μm-thick substrate) for opto-electronic devices. When two materials are bonded together, the difference of behavior under specific loading, such as thermal loading, can induce incompatible strains resulting in internal stresses [1]. The resulting stresses in the film can be sufficiently high to cause damage and failure in the film and/or the underlying substrate [2, 3, 4], or delamination and fracture along the interface [5, 6, 7, 8, 9, 10, 11, 12]. Therefore, predictions and measurements of the stresses in the film are of great importance in terms of reliability of the system. Incompatible strains in the film due to mismatch from the substrate cause a film-substrate system to bend. For this reason, measurement of the curvature of the system, which is correlated to the bending moment of the system, can be used to determine the mismatch stress in the film. Stoney (1909) derived a simple equation relating curvature of the film-substrate system, κ_{Stoney}, to stress in the film, σ_{f}, as [13]

$$\kappa_{Stoney} = \frac{6}{\overline{E_{\mathrm{s}}}} \frac{\sigma_{\mathrm{f}} h_{\mathrm{f}}}{h_{\mathrm{s}}^2}, \tag{1.1}$$

where $\overline{E_s}$ is the biaxial modulus ($E_s/[1-\nu_s]$) of the substrate, and h_f and h_s are thicknesses of the film and the substrate, respectively. The key assumptions of this simple analysis include [14]:

- the properties of the film-substrate system are such that the film material contributes negligibly to the overall elastic stiffness of the system;
- the film and the substrate have isotropic material properties in a range of linear elastic behavior;
- the curvature and in-plane strain of the substrate midplane are spatially uniform;
- all components of the displacement gradient are very small compared to unity, so that the linear elasticity theory holds;
- localized edge effects around the periphery of the film are ignored.

This simple equation, based on small deformation theory, enables the calculation of film stress without knowledge of properties of the thin film, and has been used widely in a variety of applications where a uniform film is deposited on a thicker substrate [15, 16, 17, 18, 19, 20, 21, 22] and modified to extend up to multilayer structures with or without compositional gradients[23, 24, 25].

In the micro-electronics and micro-electromechanical systems (MEMS) industries, thin metal films are patterned into a series of lines by removing unnecessary portions of an initially deposited blanket film. These lines provide a path for electrons to connect devices within a computer chip, and are termed interconnects. For the purpose of realizing faster and denser micro-electronic circuits, interconnect line width has been decreased steadily to the present submicron regime of 0.13μm, and is targeted to approach tens of nm in the near future [26]. As this decrease in line width challenges the current limits of manufacturability and reliability of the structure, mechanical integrity of these interconnects must be assessed accurately. The knowledge

of stress levels in the lines enables the assessment of the reliability of the interconnect materials against failure from such phenomena as electromigration [27, 28, 29], stress-induced voiding [30, 31] and hillock formation [32]. As new insulating materials with low dielectric constants are being introduced, new failure mechanisms are also being investigated, such as yielding and cracking in the dielectric layer embedding the metal lines [33].

One of the major factors affecting reliability is stress from thermal mismatch between metal lines and surrounding materials. Various experimental techniques such as X-ray experiments [34] and curvature measurements [35, 36, 37] have been conducted on metal lines embedded within dielectric materials. Computational methods such as finite element analysis (FEA) have been employed to obtain the stress distribution as well as volume-averaged stresses in the lines due to thermal mismatch [38, 39, 40]. Although FEA can incorporate detailed descriptions of geometry and material properties of the metal lines [40], this approach usually requires intensive computation, and must be repeated for each small change in line geometry. In contrast, analytical formulations provide predictive capabilities and reasonably accurate results in a time-effective manner [41, 42, 43]. Eshelby's inclusion theory can incorporate aspect ratios of the lines, but fails to capture the effects of a substrate and neighboring lines, and also does not consider sharp edges/corners of the lines [41, 42]. Wikström *et al.* [43] proposed an analytical model for volume-averaged stresses in lines in two limiting cases, low and high line aspect ratios. However, this analysis does not take into account substrate deformation, so it cannot provide wafer curvature information.

Since interconnect lines are typically aligned in a particular direction, stresses in the lines and deformation of the line-substrate system are no longer equibiaxial due to geometrical anisotropy, even if material properties of the lines and substrate are isotropic. Wikström *et al.* [44] modeled periodic patterned lines on a substrate as a plate with periodic surface cracks. This model, along with an anisotropic Stoney formulation, enables the evaluation of curvature changes of the line-substrate system

as well as the corresponding stress relaxation in lines which results from removal of material between lines. Due to the difficulty of etching Cu, a new fabrication technique called the Damascene process has been introduced in the semiconductor industry [45]. In this method, trenches whose dimensions conform to the geometry of the Cu interconnect lines in the circuit are dry-etched in an oxide layer which is grown on the silicon substrate. These trenches are then plugged with copper by recourse to chemical vapor deposition (CVD) or electroplating; excess Cu above the trenches is removed by chemical-mechanical polishing (CMP). The control of wafer curvature becomes critical for uniform polishing over the entire wafer. Recent analysis of this constrained copper structure has been developed by recourse to a composite analogy to capture curvature changes during fabrication steps and subsequent thermal cycling [46]. An anisotropic Stoney formulation is used again to extract volume-averaged stresses in normal directions in each Cu and dielectric line from curvature information with additional conditions in limiting cases where lines are sufficiently tall, which agrees with current trends in the microelectronics industry [47].

In addition to the aforementioned trend toward smaller line features, the drive for more cost-efficient computer chip manufacturing has motivated the microelectronic industry to fabricate larger Si wafers on which a greater number of chips can be made. Presently, the semiconductor industry is retooling its wafer fabrication facilities to accormodate 300-mm (12-inch) diameter Si wafers, instead of the current standard: 200-mm wafers [26]. This increase in wafer diameter is also accompanied by a growing trend to introduce more levels of metallization on the Si substrate which, in turn, will result in a higher effective membrane force, $\sigma_f \times h_f$, in the multi-level, thin film arrangement on the substrate. When the out-of-plane deflection of the film-substrate system is comparable to its thickness, the moderate rotation of the plate leads to a highly non-linear relationship between the strain and the displacement. This non-linearity allows for abrupt changes in shape from a spherical to an ellipsoidal shell upon bifurcation, even when film stress is uniform in-plane. As a consequence of small deformation assumptions inherent to the Stoney formula, the diameter is not

accounted for, but large deformation theory accounts for this extra in-plane length dimension.

Dimensional analysis and computational modeling of large deformation in the thin film-substrate system indicate that for fixed substrate diameter, film mismatch stress and film thickness, there exists a critical thickness of the substrate above which curvature bifurcation is suppressed [48, 49, 50, 51, 52, 53, 54, 55]. When a wafer undergoes large deformation, curvatures are no longer uniform over the entire wafer, even for a uniform film membrane force [53, 54] and are also affected by body forces such as gravity [55]. Large deformation and bifurcation have been observed with different curvature measurement techniques. Finot *et al.* [53] investigated thin W films on Si wafers, the backsides of which were polished to induce large deformation. Non-uniform curvature values were measured along the wafer diameter over a range of film membrane force and substrate geometries with a laser scanning method. The grid reflection technique, which projects a grid on the surface of wafers then collects a reflected image containing information on out-of-plane displacement of the surface, was also employed to capture bifurcation behavior [53]. Lee *et al.* [56] found nonlinear deformation in thin Al films on ultra thin (105μm) Si wafers during thermal cycling using coherent gradient sensing (CGS) technique, which measures the gradient of the out-of-plane displacement of the surface. Using this vibration-insensitive technique, shear (or twist) curvature components as well as principal curvatures were obtained for different combinations of substrate geometry and film membrane forces [57].

In this thesis, a combined analytical and numerical method is presented to evaluate curvature and stress evolution in metal and dielectric lines in an interconnect structure on a Si substrate during thermal loading. Experimental results are discussed in terms of the limitation of the small deformation theory upon which the Stoney formula is predicated. Mismatch stresses in thin films/lines and consequent curvature evolution of the film/line-substrate system are investigated in realistic, complex geometries relevant to industrial trends, such as high line aspect ratios, multi-level structures, and large diameter wafers. Additional dimensional length scales

such as line width in interconnect structures and wafer size in large deformation are taken into account to solve scientific and practical problems encountered in the field of thin film mechanics. In particular, this analysis seeks to incorporate anisotropy and non-linearity arising from geometrical changes such as directional patterning and large deformation in the range of isotropic and linear-elastic material behavior. The objectives of this thesis are as follows:

- to derive closed-form solutions for curvature evolution of the Damascene-processed line structure on a Si substrate during fabrication steps and subsequent thermal cycling;
- to obtain analytical predictions for volume-averaged stresses in metal and dielectric lines based on curvature evaluation for the purpose of developing an engineering map for selection of materials and design optimization;
- to analyze the variation of stress distribution in different metallization levels using full, 3-D finite element analysis (FEA);
- to conduct experiments with samples undergoing large deformation via the CGS technique, in order to identify the limitations of small deformation theory;
- to visualize experimentally catastrophic shape change upon bifurcation by capturing normal and twist curvature evolution;
- to obtain a full-field curvature map for probing localized curvature variation via image processing of CGS interferograms.

The thesis is organized in the following manner. Chapter 2 presents composite analogy of Damascene-processed Cu lines between dielectric trenches for evaluation of curvature changes. In Chapter 3, this composite analogy is extended to a closed-form solution for volume-averaged stresses in metal and dielectric lines, and a numerical model for multi-level structure in different line arrangements is also presented. In Chapter 4, experimental results are discussed to identify the limitations of small

deformation theory using the coherent gradient sensing technique, an optical, full-field, vibration-insensitive method. Parts of this work have already been published in [46] and prepared for publication in [47, 57].

Chapter 2

Curvature Modeling of Damascene-Processed Lines on Substrates

A simple theoretical analysis for curvature evolution in unpassivated and passivated copper interconnect lines on a silicon substrate is proposed in this chapter. A layer consisting of copper and oxide lines is modeled as a homogenized composite which has different elastic moduli and thermal expansion coefficients in two different directions, i. e., along and across the lines, due to the anisotropic line geometry. These effective thermoelastic properties of the composite layer are approximated in terms of volume fractions and thermoelastic properties of each line using standard composite theory. This analogy facilitates the calculation of curvature changes in Damascene-processed copper lines subjected to chemical-mechanical polishing and/or thermal cycling. The effects of line height, width and spacing on curvature evolution along and across the lines are readily extracted from the analysis. In addition, this theory is easily extended to passivated copper lines irrespective of passivation materials by superimposing the curvature change resulting from an additional layer. Finite element analysis has been used to assess the validity of the theoretical predictions; such comparisons show that the simple theory provides a reasonable match with numerical simulations of curvature evolution during the Damascene process in copper interconnects for a wide range of

line and passivation geometry of practical interest.

2.1 Introduction

The reliability of metal interconnect lines in integrated circuits is known to be influenced by failure mechanisms such as electromigration [27, 28, 29] and stress-induced voiding [30, 31, 35]. In ultra large scale integration (ULSI) devices, multilevel metallization is needed. Oxide passivation layer deposition usually involves heating up to 400°C so that the interconnect lines undergo several thermal cycles. Thermal stresses are generated by the large difference in expansion/contraction which develops between the metal interconnect lines and surrounding materials during thermal cycling. Tensile thermal stresses formed during cooling from the oxide deposition temperature can cause voiding near the interface between an interconnect line and the surrounding passivation layer.

Due to the difficulty of etching copper, a new fabrication technique called the Damascene process has been introduced in the semiconductor industry [58]. In this method, trenches whose dimensions conform to the geometry of the copper interconnect lines in the circuit are dry-etched in an oxide layer which is grown on the silicon substrate. These trenches are then plugged with copper by recourse to chemical vapor deposition (CVD) or electroplating. The extra copper above the trenches is then removed by chemical-mechanical polishing (CMP), and then a passivation or capping layer is deposited on top of the interconnect structure. As this process involves polishing, the control of curvature of the silicon wafer becomes critical for uniform polishing over the entire wafer. The changes in curvature induced during polishing and subsequent passivation also provide valuable information about the evolution of internal stresses in the interconnect lines. The objective of this work was to develop a simple theoretical analysis of the evolution of curvature along and across copper interconnect lines on silicon substrates during various fabrication steps, as functions

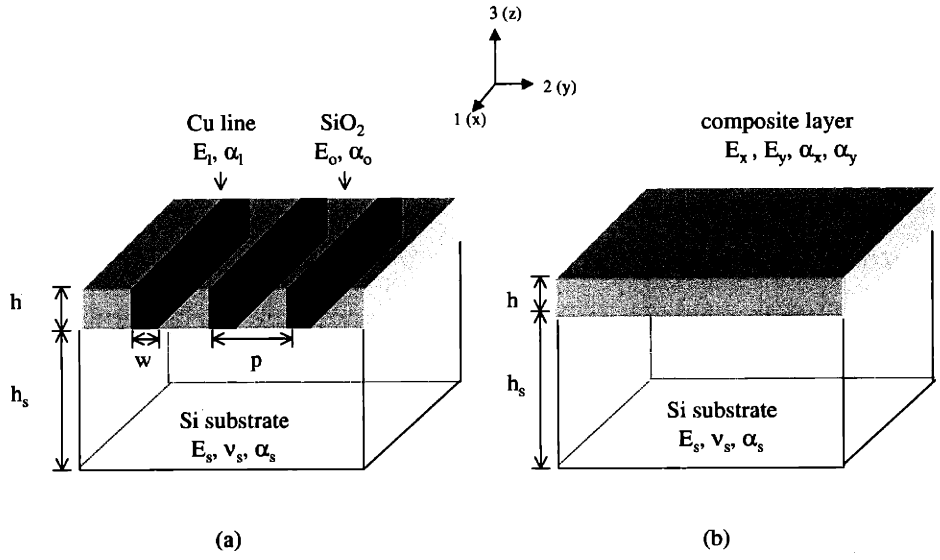

Figure 2-1: Schematic of unpassivated Cu interconnect lines on a Si substrate following Damascene process (a) individual Cu lines and SiO_2 lines (b) homogenized composite layer.

of the line and passivation geometry. The analytical results are verified with numerical simulation using the finite element method (FEM) for a range of line geometry of practical interest.

2.2 Analytical Model

Figure 2-1(a) is a schematic of Cu interconnect lines on a Si substrate following the Damascene process. Assuming that the aspect ratio (h/w) of the Cu and SiO_2 lines is high (typically equal to or greater than unity), the structure can be homogenized into a composite layer as shown in Fig. 2-1(b). Due to the anisotropic line geometry, this composite layer has different values of effective elastic modulus and thermal expansion

coefficient along the lines, E_x and α_x, respectively, than those across the lines, E_y and α_y, respectively, even if Cu itself is modeled as elastically and thermally isotropic. Using composite theory, these effective properties can be calculated in terms of the volume fraction, elastic modulus and thermal expansion coefficient of Cu lines, f_l (= w/p), E_l and α_l, and those of SiO_2 lines, f_o (= 1 – w/p), E_o and α_o.

Considering an anisotropic plate of an elastic material which is subjected to bending moments, M_x and M_y, along the x and y directions, respectively, where x–y is the plane of the plate, the resulting non-equibiaxial stress are generally expressed as [59],

$$M_x = \langle \sigma_{xx} \rangle \, h \left(\frac{h_s}{2} \right) = -\frac{E_s h_s^3}{12(1-\nu_s^2)} (\kappa_x + \nu_s \kappa_y), \tag{2.1}$$

$$M_y = \langle \sigma_{yy} \rangle \, h \left(\frac{h_s}{2} \right) = -\frac{E_s h_s^3}{12(1-\nu_s^2)} (\kappa_y + \nu_s \kappa_x), \tag{2.2}$$

where $\langle \sigma_{xx} \rangle$ and $\langle \sigma_{yy} \rangle$ are the normal stresses in the plate along the x and y directions, respectively, κ_x and κ_y are the curvatures along the x and y directions, respectively, and E_s and ν_s are the elastic modulus and Poisson ratio, respectively, of the Si substrate. Equations (2.1) and (2.2) can be rewritten as,

$$\kappa_x = -\frac{6}{E_s} \frac{h}{h_s^2} \left[\langle \sigma_{xx} \rangle - \nu_s \langle \sigma_{yy} \rangle \right], \tag{2.3}$$

$$\kappa_y = -\frac{6}{E_s} \frac{h}{h_s^2} \left[\langle \sigma_{yy} \rangle - \nu_s \langle \sigma_{xx} \rangle \right]. \tag{2.4}$$

From Eqs. (2.3) and (2.4), it is evident that the curvature in one direction is expected to have some contribution from the thermal stress resulting from thermal mismatch in the other direction. This coupling term, however, includes the Poisson ratio, which makes this contribution relatively small. In addition coupling can be taken into account by considering the effective thermal expansion coefficients of the homogenized composite layer, which somewhat compensates for the limitations of a

one-dimensional approach. It could, therefore, be postulated that a simple uniaxial, anisotropic composite model for a patterned elastic lines might provide sufficiently accurate predictions of curvature evolution in response to changes in geometry (such as that arising from chemical-mechanical polishing) or to changes in internal stresses arising from thermal cycling. A simple analytical model for curvature evolution in unpassivated and passivated interconnect lines is developed on the basis of this premise. The conditions of validity of such a simple model are then assessed using detailed finite element simulations.

The volume-averaged stress from thermal mismatch in uniaxial state is approximated as,

$$\langle \sigma_{xx} \rangle = -E_x \left(\alpha_x - \alpha_\mathrm{s} \right) \Delta T, \qquad \langle \sigma_{yy} \rangle = -E_y \left(\alpha_y - \alpha_\mathrm{s} \right) \Delta T. \tag{2.5}$$

Combining Eq. (2.5) with Eq. (2.3) or (2.4), the curvature components are calculated to be,

$$\kappa_x = \frac{6}{E_\mathrm{s}} \frac{h}{h_\mathrm{s}^2} E_x (\alpha_x - \alpha_\mathrm{s}) \Delta T, \qquad \kappa_y = \frac{6}{E_\mathrm{s}} \frac{h}{h_\mathrm{s}^2} E_y (\alpha_y - \alpha_\mathrm{s}) \Delta T. \tag{2.6}$$

Equation (2.6), which is valid only for uniaxial loading, is used for calculating curvature evolution of the homogenized composite layer consisting of Cu and SiO_2 lines which is subjected to biaxial loading.

The volume-averaged stresses from thermal mismatch in equibiaxial state are expressed as,

$$\langle \sigma_{xx} \rangle = \langle \sigma_{yy} \rangle = -\overline{E_\mathrm{f}} \left(\alpha_\mathrm{f} - \alpha_\mathrm{s} \right) \Delta T, \tag{2.7}$$

where $\overline{E_\mathrm{f}}$ and α_f are the biaxial modulus ($E_\mathrm{f}/[1-\nu_\mathrm{f}]$) and thermal expansion coefficient, respectively, of a uniform film. Combining Eq. (2.7) with Eqs. (2.3) and (2.4), the curvatures can be found as,

$$\kappa_x = \kappa_y = \frac{6}{\overline{E_\mathrm{s}}} \frac{h}{h_\mathrm{s}^2} \overline{E_\mathrm{f}} (\alpha_\mathrm{f} - \alpha_\mathrm{s}) \Delta T, \tag{2.8}$$

where $\overline{E_\mathrm{s}}$ and α_s are the biaxial modulus ($E_\mathrm{s}/[1-\nu_\mathrm{s}]$) and thermal expansion coeffi-

cient, respectively, of the Si substrate. Equation (2.8) is used for curvature evolution of the uniform passivation layer, which is a continuous SiO_2 layer in this work.

2.2.1 Unpassivated Lines

The total strains during thermal excursions are the same along the Cu and SiO_2 lines, and they are related to the effective thermal expansion coefficient along the lines as,

$$\alpha_x \Delta T = \frac{\langle \sigma_l \rangle}{E_l} + \alpha_l \Delta T = \frac{\langle \sigma_o \rangle}{E_o} + \alpha_o \Delta T, \tag{2.9}$$

where $\langle \sigma_l \rangle$ and $\langle \sigma_o \rangle$ are the volume-averaged stresses in the Cu and SiO_2 lines, respectively. A force balance equation for this geometry gives,

$$f_l \langle \sigma_l \rangle + f_o \langle \sigma_o \rangle = 0. \tag{2.10}$$

From Eqs. (2.9) and (2.10), the effective thermal expansion coefficient along the line direction is,

$$\alpha_x = \frac{f_l E_l \alpha_l + f_o E_o \alpha_o}{f_l E_l + f_o E_o}. \tag{2.11}$$

The effective elastic modulus along the line direction is written, using the composite theory, as

$$E_x = f_l E_l + f_o E_o. \tag{2.12}$$

Substituting E_x and α_x from Eqs. (2.11) and (2.12) for the corresponding properities in Eq. (2.6), the curvature change along the lines, κ_x, is found to be,

$$\kappa_x = \frac{6}{E_s} \frac{h}{h_s^2} E_x (\alpha_x - \alpha_s) \Delta T. \tag{2.13}$$

Across the lines, consideration of thermal expansion in the line and of the

Poisson effect gives,

$$\alpha_y \Delta T = f_l \left[-\nu_l \frac{\langle \sigma_l \rangle}{E_l} + \alpha_l \Delta T \right] + f_o \left[-\nu_o \frac{\langle \sigma_o \rangle}{E_o} + \alpha_o \Delta T \right]. \tag{2.14}$$

Substituting $\langle \sigma_l \rangle$ and $\langle \sigma_o \rangle$ from Eqs. (2.9) and (2.10) into Eq. (2.14), the effective thermal expansion coefficient across the line direction is calculated as,

$$\alpha_y = f_l \alpha_l + f_o \alpha_o + \frac{f_l f_o (\nu_l E_o - \nu_o E_l)(\alpha_l - \alpha_o)}{f_l E_l + f_o E_o}. \tag{2.15}$$

The effective elastic modulus across the line direction is written, with standard composite theory, as

$$E_y = \frac{E_l E_o}{f_l E_o + f_o E_l}. \tag{2.16}$$

Substituting E_y and α_y from Eqs. (2.15) and (2.16) into Eq. (2.6), the curvature change across the lines, κ_y, becomes

$$\kappa_y = \frac{6}{E_s} \frac{h}{h_s^2} E_y (\alpha_y - \alpha_s) \Delta T. \tag{2.17}$$

Wikström *et al.* [43] derived expressions for the normal components of volume-averaged stresses in interconnect lines for two limiting cases: very low and high line aspect ratios, h/w. At a very low line aspect ratio, $h/w \to 0$, the interconnect structure can be considered as comprising individual Cu and SiO_2 films. Therefore, the curvature changes in both directions, i.e. along and across the lines, are the same and are obtained by adding the appropriate contribution from each film;

$$\kappa_x^{\text{low}} = \kappa_y^{\text{low}} = -6 \frac{h}{h_s^2} \frac{1 - \nu_s}{E_s} \left[f_l \langle \sigma_l \rangle^{\text{low}} + f_o \langle \sigma_o \rangle^{\text{low}} \right], \tag{2.18}$$

where $\langle \sigma_l \rangle^{\text{low}}$ and $\langle \sigma_o \rangle^{\text{low}}$ are the volume-averaged biaxial stresses in the lines and the oxide, respectively, for the case of the low line aspect ratio. Similarly, κ_l^{low} and κ_o^{low} are the curvatures in the Cu and SiO_2 films, respectively.

As integration of the devices increases with decreasing line width, the aspect

ratio of interconnect lines currently used in the semicondutor industry is also increased. At high line aspect ratios, $h/w \geq 1$, the curvature changes in each direction are obtained as follows;

$$\begin{bmatrix} \kappa_x^{\text{high}} \\ \kappa_y^{\text{high}} \end{bmatrix} = -6\frac{h}{h_s^2}\frac{1}{E_s}\begin{bmatrix} 1 & -\nu_s \\ -\nu_s & 1 \end{bmatrix}\begin{bmatrix} f_l \left\langle \sigma_{xx}^l \right\rangle^{\text{high}} + f_o \left\langle \sigma_{xx}^o \right\rangle^{\text{high}} \\ f_l \left\langle \sigma_{yy}^l \right\rangle^{\text{high}} + f_o \left\langle \sigma_{yy}^o \right\rangle^{\text{high}} \end{bmatrix}, \tag{2.19}$$

where the superscript 'high' denotes the high line aspect ratio for the components of volume-averaged stresses and curvatures in the Cu and SiO_2 lines in this regime. At $f_l = f_o = 0.5$, Eqs. (2.13) and (2.17) give approximate values with less than 5% error compared to the values from Eq. (2.19). Therefore, the present model shows a reasonably good match in the range of practical line geometry, $h/w \geq 1$, in spite of its simplifying assumption that the curvatures along and across the line direction do not influence one another.

2.2.2 Passivated Lines

The evolution of curvatures in passivated elastic Cu interconnect lines can also be assessed using the above simple model by invoking the concept of superposition. Figure 2-2 shows a schematic of passivated Cu lines, which can be regarded as superimposition of the composite layer and the passivation layer. For a given passivation material, the curvature change resulting from the passivation layer, κ_p, is obtained in terms of the biaxial modulus of the passivation layer, $\overline{E_p}$ $(= E_p/[1-\nu_p])$, its thermal expansion of coeffiecient, α_p, and its thickness, h_p, using Eq. (2.8) as,

$$\kappa_p = \frac{6}{\overline{E_s}}\frac{h_p}{h_s^2}\overline{E_p}(\alpha_p - \alpha_s)\Delta T. \tag{2.20}$$

By adding κ_p from Eq. (2.20) to κ_x and κ_y from Eqs. (2.13) and (2.17) respectively, curvature changes of passivated lines, κ_x' and κ_y', are obtained:

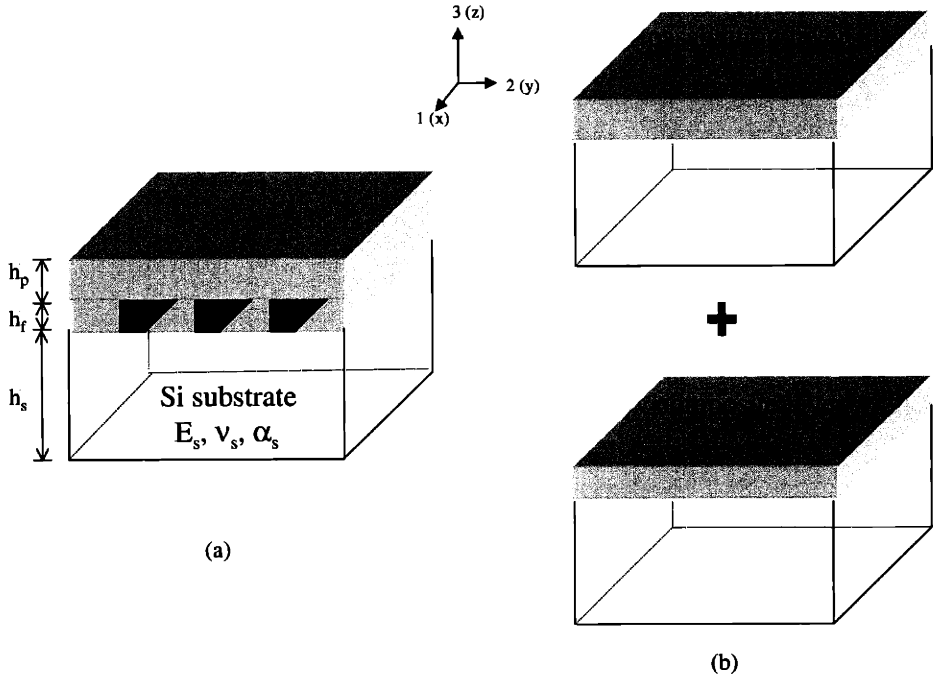

Figure 2-2: Schematic of passivated Cu interconnect lines on a Si substrate following passivation (a) actual interconnect structure (b) superimpostion of the composite layer and passivation layer.

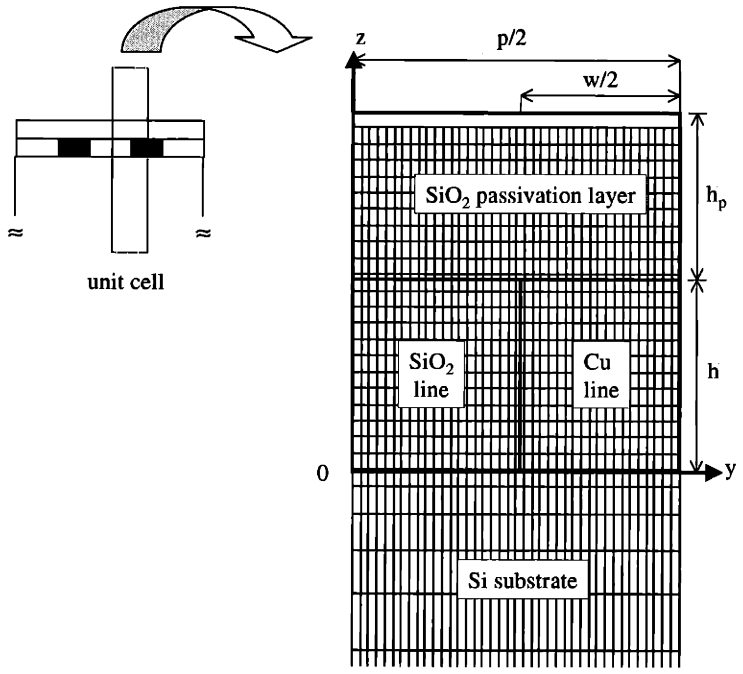

Figure 2-3: A representative unit cell (top portion) and finite element discretization for Cu lines in the Damascene process.

$$\kappa_x^{'} = \kappa_x + \kappa_{\mathrm{p}} = \frac{6}{E_{\mathrm{s}}}\frac{h}{h_{\mathrm{s}}^2}E_x(\alpha_x - \alpha_{\mathrm{s}})\Delta T + \frac{6}{\overline{E_{\mathrm{s}}}}\frac{h_{\mathrm{p}}}{h_{\mathrm{s}}^2}\overline{E_{\mathrm{p}}}(\alpha_{\mathrm{p}} - \alpha_{\mathrm{s}})\Delta T. \tag{2.21}$$

$$\kappa_y^{'} = \kappa_y + \kappa_{\mathrm{p}} = \frac{6}{E_{\mathrm{s}}}\frac{h}{h_{\mathrm{s}}^2}E_y(\alpha_y - \alpha_{\mathrm{s}})\Delta T + \frac{6}{\overline{E_{\mathrm{s}}}}\frac{h_{\mathrm{p}}}{h_{\mathrm{s}}^2}\overline{E_{\mathrm{p}}}(\alpha_{\mathrm{p}} - \alpha_{\mathrm{s}})\Delta T. \tag{2.22}$$

2.3 Finite Element Analysis

The finite element method (FEM) was used to verify the present analytical model. For this purpose, the general purpose finite element program ABAQUS [60] was employed.

Table 2.1: Material properties used in the simulations.

	E (GPa)	ν	α (10^{-6} / °C)
Si	130	0.28	2.60
Cu	110	0.30	17.0
SiO_2	71.4	0.16	0.524

The mesh used in the present numerical simulation is shown in Fig. 2-3. Due to the periodicity and symmetry of the arrangement, only a unit segment ranging from a symmetric axis and the neighboring periodic boundary is needed. Here h, w and p represent the height, width, and spacing of Cu lines, respectively. A generalized plane strain formulation, which is an extension of the plane strain framework (with the y-z plane being the plane of deformation), was used in the calculations. This was accomplished by superimposing a longitudinal strain, ϵ_{xx}, on the plane strain state. The detailed procedure for obtaining the curvatures using such numerical simulation can be found in earlier papers [38, 39].

Table 2.1 shows the material properties used in the simulations [39, 44]. Isotropic material properties were used, and residual stresses which may result from Cu deposition and/or polishing were not taken into account. This analysis deals with only elasticity, which is expected to be valid over a wide range of practical interest since the material surrounding the Cu lines, especially in case of passivated lines, leads to elevated levels of hydrostatic stress in the lines thereby inducing constrained deformation [35].[1]

[1]In the unpolished Cu layer (before CMP), however, plastic deformation can occur because the yield strength of unpassivated Cu films can be very low at moderate temperature (well below 400°C) [61]. Unpassivated Cu lines (after CMP) which are in the trench with its top face being free may also plastically deform due to high deviatoric components unless the aspect ratio is very high. These inelastic deformations should be considered when experimental data are compared to the present model.

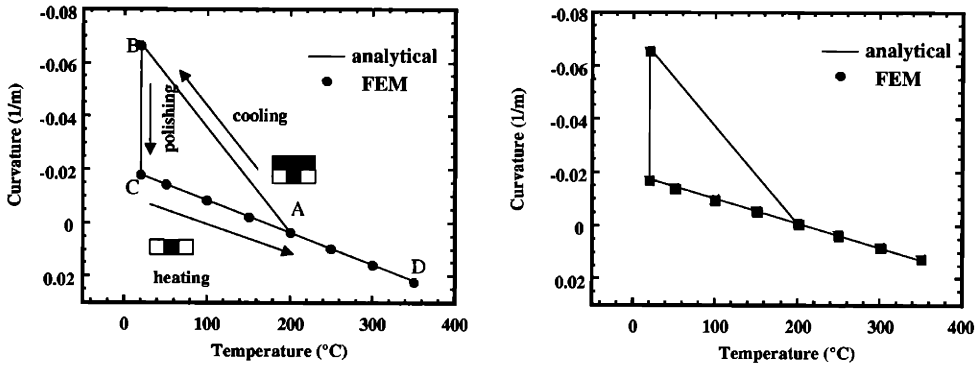

Figure 2-4: Curvature changes of unpassivated Cu lines in the Damascene process at fixed line geometry ($h = 1\mu m$, $h_s = 525\mu m$, $h/w = 1$, $p/w = 2$). The Cu layer is deposited at 200°C (a) along lines (b) across lines.

2.4 Results and Discussion

2.4.1 Changes in Curvature during the Damascene Process

Figure 2-4(a) shows curvature changes along the unpassivated Cu lines from the Damascene process for a fixed line geometry ($h/w = 1$, $p/w = 2$). First we assume that the SiO_2 layer is grown by thermal oxidation at 1000°C, cooled down to 200°C, and then patterned into trenches (at A). The residual stress formed during oxidation is not considered in this simulation. At 200°C, a Cu layer is deposited on patterned SiO_2 lines, and then cooled down to room temperature (A→B). A very large curvature change occurs during cooling in this direction. When an excess Cu layer is removed by polishing (B→C), the curvature drops drastically. Then as the temperature is raised

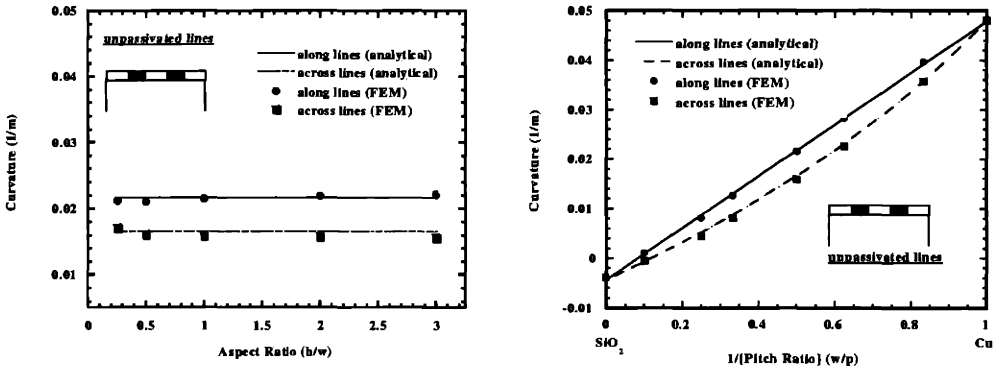

(a) (b)

Figure 2-5: Curvature changes of unpassivated Cu lines ($h = 1\mu m$, $h_s = 525\mu m$) during heating from room temperature to 200°C as a function of (a) aspect ratio at fixed pitch ratio ($p/w = 2$) (b) reciprocal of pitch ratio at fixed aspect ratio ($h/w = 1$).

from room temperature (C→D), the curvature changes in the opposite direction. Across the lines, Fig. 2-4(b), the curvarture change shows different slopes from those along lines during cooling and heating. Analytical predictions are exactly matched with calculated values by FEM in both directions during the above fabrication and thermomechanical processes.

2.4.2 Effects of Line and Passivation Geometry

Figure 2-5(a) shows curvature changes during heating from room temperature to 200°C as a function of aspect ratio at a fixed pitch ratio ($p/w = 2$). When the pitch

ratio is fixed, the fraction of Cu in this composite layer is unchanged. Therefore Eqs. (2.13) and (2.17) give constant curvature values, which reasonably fit the results of numerical simulation over a wide range.

Figure 2-5(b) shows curvature changes during heating from room temperature to 200°C as a function of the reciprocal of pitch ratio (w/p), which corresponds to the volume fraction of Cu, at fixed aspect ratio ($h/w = 1$). As the spacing between the Cu lines increases, the fraction of Cu in this layer decreases. Considering the volume fraction in the Eqs. (2.13) and (2.17), analytical values agree closely with FEM results over all the Cu volume fraction in the layer which consists of Cu and SiO_2 lines. When a pure Cu film is considered ($w/p \rightarrow 1$), the present one-dimensional model gives,

$$\kappa_x = \kappa_y = \frac{6}{E_s}\frac{h}{h_s^2}E_l(\alpha_l - \alpha_s)\Delta T. \tag{2.23}$$

However, biaxial modulus of the Cu film and the Si substrate should be used to obtain exact curvature changes for this two-dimensional structure:

$$\kappa_x^{\text{exact}} = \kappa_y^{\text{exact}} = \frac{6}{\overline{E_s}}\frac{h}{h_s^2}\overline{E_l}(\alpha_l - \alpha_s)\Delta T = \left[\frac{1-\nu_s}{1-\nu_l}\right]\frac{6}{E_s}\frac{h}{h_s^2}E_l(\alpha_l - \alpha_s)\Delta T. \tag{2.24}$$

Therefore the factor of $(1-\nu_s)/(1-\nu_l)$ can be regarded as an error of the present model in this limiting case, and it gives only 3% error for the pure Cu film. In the same way, corresponding factor for a pure SiO_2 film, ($w/p \rightarrow 0$), can be expressed as $(1-\nu_s)/(1-\nu_o)$, which shows a 17% error. But since this SiO_2 rich region shows very small curvature changes compared to that with high Cu volume fraction, this error is not large in an absolute value. Therefore it shows a very good agreement with numerical simulation in a fairly wide range, where practical interconnect line geometries lie.

Analytical predictions and FEM results for passivated lines with SiO_2 passivation layer are shown in Fig. 2-6. They represent almost the same trends as unpassivated lines with smaller absolute values because the thermal expansion coef-

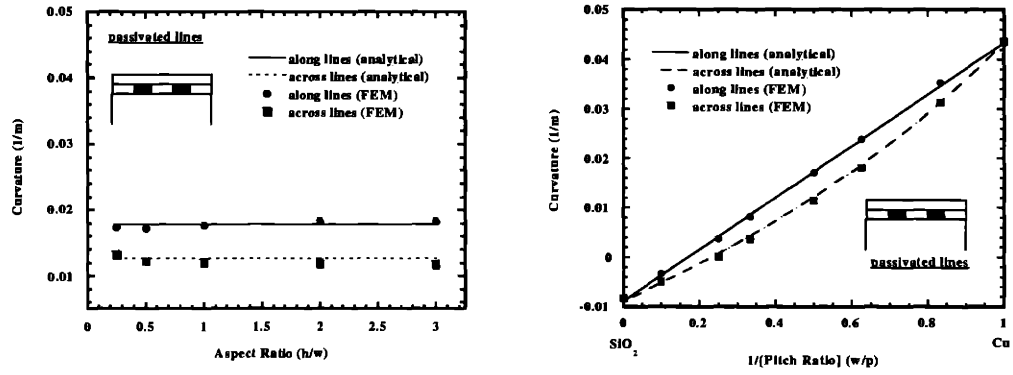

(a) (b)

Figure 2-6: Curvature changes of passivated Cu lines with SiO_2 passivation layer ($h = 1\mu m$, $h_p = 1\mu m$, $h_s = 525\mu m$) during heating from room temperature to 200°C as a function of (a) aspect ratio at fixed pitch ratio ($p/w = 2$) (b) reciprocal of pitch ratio at fixed aspect ratio ($h/w = 1$).

ficient of oxide is lower than Si substrate. Due to the high diffusivity of Cu through SiO_2 and Si, a diffusion barrier such as TaN is commonly employed [58]. Although it makes more complicated interconnect structures, the effect of this additional layer can be easily incorporated in the present model by superimposition for linear elasticity condition and may be negligible if this layer is very thin, i.e. order of a few hundred Å.

2.5 Conclusions

In this paper, a simple analytical model based on a composite analogy has been used to predict curvature in unpassivated and passivated Cu lines in Damascene process. A layer consisting of copper and oxide lines is modeled as a homogenized composite layer consisting of Cu and SiO_2 lines. The effective thermoelastic properties of the composite layer are computed in terms of volume fractions and thermoelastic properties of each line using standard composite theory, which enables us to calculate curvature changes during the Damascene process employing thermal cycling and polishing. Finite element analyses have been used to assess the accuracy of the simple analytical model. These values are exactly matched with each other during Cu deposition, polishing, passivation, and thermal cycling under the assumption of isotropic material properties and linear elasticity conditions. Although residual stresses are not incorporated into the analyses, they can be appropriately superimposed to modify the predicted curvatures if the magnitudes of residual stresses are known. The effects of line geometry such as aspect ratio, h/w, and pitch ratio, p/w, can also be rationalized with the present model. In addition, the model can also be easily extended to include passivated copper lines, for any passivation material, by superimposing the curvature change resulting from an additional layer.

Chapter 3

Stress Modeling of Lines in Single- and Multi-level Structures

A simple analysis of curvature and thermal stress evolution in single- and multi-level interconnect line structures on a substrate is presented in this chapter. Two limiting line structures are considered. When the line is very wide compared to its height, each metal and dielectric line behaves like an individual thin film in an equibiaxial plane stress state. When lines are sufficiently tall, on the other hand, the line structure is homogenized into a single composite layer with different effective thermoelastic properties along and across the lines due to geometrical anisotropy. Effects of passivation geometry and stiffness on the stress evolution in the lines are also presented. Since theory predicts stress values as a function of spacing between metal lines as well as line aspect ratio, interactions between neighboring lines on the same level can be analyzed. A 2-D finite element method using a generalized plane strain model has been used to verify the validity of the current model, while available experimental data on stresses and curvatures of the line structure were compared to the current theory. In order to capture the variation of the thermal stresses on different metalization levels, as well as the effect of the upper level line arrangements on the stress states in the lower level, a 3-D finite element analysis was

employed. Interaction between levels in the vertical direction will be investigated and the applicability of curvature and stress modeling based on the single-level to the multi-level structure will be discussed.

3.1 Introduction

It is desirable to evaluate stresses in interconnect lines formed on a Si substrate to improve the design of the device structure, selection of materials, fabrication processes and other aspects of the device to enhance its manufacturability and reliability. Stress measurements can be used to facilitate quality control of the mechanical integrity during various fabrication steps including film deposition, patterning, polishing and thermal cycling. Determining the stress values in the lines also enables us to assess the reliability of the interconnect materials against failure from such phenomena as electromigration [27, 28, 29], stress-induced voiding [30, 31] and hillock formation [32]. As new insulating materials with low dielectric constants are introduced, additional failure mechanisms, such as yielding and cracking in the dielectric layer embedding the metal lines, are also being investigated [33].

The stresses in the interconnect structure may result from various sources. One of the major factors affecting reliability is the stresses resulting from thermal mismatch between metal lines and surrounding materials. Various experimental techniques such as X-ray experiments [34] and curvature measurements [35, 36, 37] were made for the metal lines embedded within the dielectric materials. For predicting thermal stress evolution in the metal lines, finite element analysis (FEA) has been employed to obtain the stress distribution as well as volume-averaged stresses [38, 39, 40]. Although it can incorporate detailed information of the metal lines, including anisotropic material properties in individual grains and/or exact geometry of passivation [40], FEA usually requires lengthy computation, and must generally be done each time the line geometry changes even slightly. Compared to FEA, analytical

predictions not only provide good insight, but also reasonably accurate results in a time-efficient manner [41, 42, 43]. Eshelby's inclusion theory can incorporate aspect ratios of the lines, but fails to capture the effects of a substrate and neighboring lines, and also does not consider sharp edges/corners of the lines [41, 42]. Wikström *et al.* [43] proposed the two limiting cases, low and high line aspect ratios, which are similar to the analysis in the present work. However, the above limiting cases do not account for substrate deformation, and therefore cannot provide wafer curvature information.

One way of determining stresses in both the embedded metal interconnect lines and the dielectric materials embedding the metal lines is by measuring the curvatures of the Si substrate on which the interconnect line structure is formed. Volume-averaged stresses in the metal and dielectric lines resulting from incompatible mismatch strains between each other and the substrate cause the wafer to bend. The correlation between wafer curvatures to volume-averaged stresses in the overlying thin structure on the substrate was first found in a uniform, homogeneous thin layer on a much thicker substrate by Stoney [13], and has since been extended to more complicated structures such as multi-layer structures [52], unpassivated line structures [44], and passivated line structures [62].

As aluminum-based interconnects are replaced with copper, a new fabrication technique known as the Damascene process involving chemical-mechanical polishing (CMP) rather than etching is being employed in the semiconductor industry [45]. Two limiting cases can be considered. When line aspect ratios are very low, each line can be considered an individual film. In contrast, when aspect ratios are sufficiently high, the metal and dielectric lines produced by the Damascene process can be modeled as a homogeneous, but anisotropic composite layer with different effective thermoelastic properties along and across the lines [46]. This enables us to calculate the curvature in each direction and to extend to line structures with an overlying passivation layer using superposition. In this work, the wafer curvatures were calculated as a function of line geometry, and the volume-averaged stresses in the lines during temperature changes were extracted in two limiting cases using the stress-curvature

relation. These analytical results were then compared to both 2-D FEA and available experimental results over a wide range of in-plane line geometry such as aspect ratio and metal density, and out-of-plane parameters such as passivation material and thickness, to evaluate the validity of the theoretical predictions. Furthermore, 3-D FEA was carried out for the purpose of capturing realistic features of multilevel structures and extending this analysis to the more complicated line geometry in the present work.

3.2 Analytical Model

3.2.1 Single-level structure

At low line aspect ratio

When metal and dielectric lines are very short (Fig. 3-1(a)), each line can be treated as an individual thin layer (Fig. 3-1(b)). Since the lines are very wide across the line direction, and the line height is very small compared to both its length and width, the stress state in the lines is basically equibiaxial plane stress. Therefore, the volume averaged stress values along the line (x-direction), and across the line (y-direction) are the same, as are the curvatures in the x- and y-directions, for this limiting line geometry. From force and moment balance equations of the metal thin layer structure [52], the volume-averaged stresses from thermal mismatch in the metal line, $\left\langle \sigma^l \right\rangle$, and the curvatures of the metal/substrate structure, κ^l , during temperature change, ΔT, can be expressed as,

$$\left\langle \sigma^l_{xx} \right\rangle = \left\langle \sigma^l_{yy} \right\rangle = -\overline{E_l}\,(\alpha_l - \alpha_{\mathrm{s}})\,\Delta T, \quad \left\langle \sigma^l_{zz} \right\rangle = 0, \tag{3.1}$$

$$\kappa^l_x = \kappa^l_y = \frac{6}{\overline{E_{\mathrm{s}}}} \frac{h}{h_{\mathrm{s}}^2} \overline{E_l} (\alpha_l - \alpha_{\mathrm{s}}) \Delta T, \tag{3.2}$$

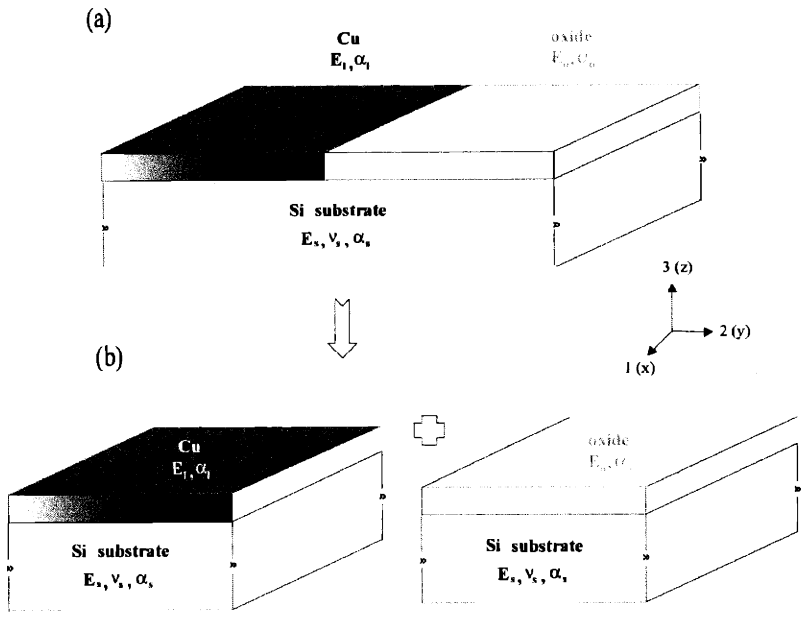

Figure 3-1: Schematic of Cu interconnect lines without a passivation layer on a Si substrate following Damascene process at low line aspect ratio.

where $\overline{E_l}$ and α_l are the biaxial modulus ($E_l/[1-\nu_l]$) and thermal expansion coefficient, respectively, of the thin metal layer, $\overline{E_s}$ and α_s are the corresponding properties of the substrate, and h and h_s are thicknesses of the layer and the substrate, respectively. The same expressions can be obtained for the volume-averaged stresses in the dielectric line, $\langle \sigma^o \rangle$, and the curvatures of the dielectric/substrate structure, κ^o , with corresponding thermoelastic properties of the dielectric lines. The overall curvatures of both the metal and dielectric layers on the substrate (Fig. 3-1(a)) are simply the sum of contributions from each layer (Fig. 3-1(b)).

At high line aspect ratio

Figure 3-2(a) is a schematic of metal interconnect lines (*e. g.* copper) with dielectric lines (*e. g.* oxide) on a Si substrate following the Damascene process. Assuming that the aspect ratio (h/w) of the metal and dielectric lines is sufficiently high, the structure can be homogenized into a composite layer as shown in Fig. 3-2(b) [43, 46]. Due to the anisotropic line geometry, this composite layer has different values of

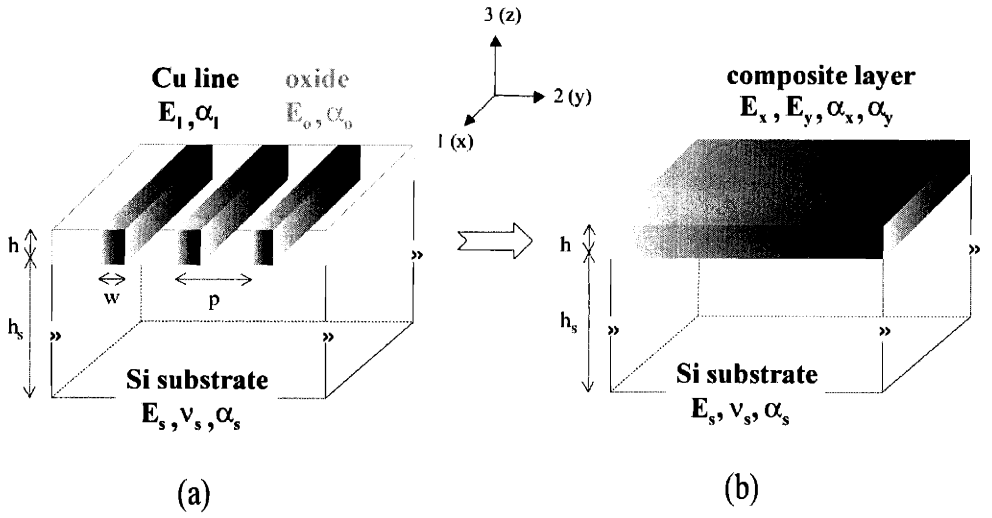

Figure 3-2: Schematic of Cu interconnect lines without a passivation layer on a Si substrate following the Damascene process at high line aspect ratio.

effective elastic modulus and thermal expansion coefficient along the lines, E_x and α_x, respectively, from those across the lines, E_y and α_y, respectively, even if the material itself is modeled as elastically and thermally isotropic. Using composite theory, these effective properties can be calculated in terms of the volume fraction, elastic modulus and thermal expansion coefficient of metal lines, f_l $(= w/p)$, E_l and α_l, and those of dielectric lines, f_o $(= 1 - w/p)$, E_o and α_o [46]. Along the lines,

$$E_x = f_l E_l + f_o E_o. \tag{3.3}$$

$$\alpha_x = \frac{f_l E_l \alpha_l + f_o E_o \alpha_o}{f_l E_l + f_o E_o}. \tag{3.4}$$

Then across the lines,

$$E_y = \frac{E_l E_o}{f_l E_o + f_o E_l}. \tag{3.5}$$

$$\alpha_y = f_l \alpha_l + f_o \alpha_o + \frac{f_l f_o (\nu_l E_o - \nu_o E_l)(\alpha_l - \alpha_o)}{f_l E_l + f_o E_o}. \tag{3.6}$$

Park and Suresh [46] proposed a simple uniaxial, anisotropic composite model for patterned elastic lines to predict curvature evolution in response to changes in internal stresses arising from thermal cycling. Their model provides reasonably ac-

curate values compared to detailed finite element analysis. The curvature changes of the wafer along and across the lines, κ_x and κ_y, respectively, during temperature change, ΔT, are expressed as,

$$\kappa_x = \frac{6}{E_s}\frac{h}{h_s^2}E_x(\alpha_x - \alpha_s)\Delta T, \tag{3.7}$$

$$\kappa_y = \frac{6}{E_s}\frac{h}{h_s^2}E_y(\alpha_y - \alpha_s)\Delta T, \tag{3.8}$$

where h and h_s are thicknesses of the layer and the substrate, respectively.

When the homogenized layer is much thinner than the substrate, the volume-averaged normal stresses in the layer along and across the lines, $\langle\sigma_{xx}\rangle$ and $\langle\sigma_{yy}\rangle$, respectively, can be obtained from curvature changes during a thermal excursion as,

$$\begin{bmatrix} \langle\sigma_{xx}\rangle \\ \langle\sigma_{yy}\rangle \end{bmatrix} = -\frac{1}{6}\frac{h_s^2}{h}\frac{E_s}{1-\nu_s^2}\begin{bmatrix} 1 & \nu_s \\ \nu_s & 1 \end{bmatrix}\begin{bmatrix} \kappa_x \\ \kappa_y \end{bmatrix}, \tag{3.9}$$

where E_s and ν_s are the elastic modulus and Poisson's ratio, respectively, of the substrate. The minus sign appears since a positive curvature change is defined in this work as the development of a concave shape, as viewed from the back side of the wafer. Eq. (3.9) is simply an anisotropic form of the well-known Stoney formula [44, 62].

The in-plane averaged stresses in the homogenized layer can be obtained from the contribution of each individual line as,

$$\langle\sigma_{xx}\rangle = f_l\left\langle\sigma_{xx}^l\right\rangle + f_o\left\langle\sigma_{xx}^o\right\rangle. \tag{3.10}$$

$$\langle\sigma_{yy}\rangle = f_l\left\langle\sigma_{yy}^l\right\rangle + f_o\left\langle\sigma_{yy}^o\right\rangle. \tag{3.11}$$

Therefore, the in-plane volume averaged stresses in the layer comprising two different lines (Eqs. (3.10), (3.11)) are related to curvatures (Eq. (3.9)), which can be expressed as functions of line geometry and the thermoelastic properties of the lines and the

substrate (Eqs. (3.3)–(3.8)). Since the thickness of the layer is much less than that of the substrate, the out-of-plane average stresses in the layer vanishes,

$$\langle \sigma_{zz} \rangle = f_l \left\langle \sigma^l_{zz} \right\rangle + f_o \langle \sigma^o_{zz} \rangle = 0. \tag{3.12}$$

Up to now an anisotropic form of the Stoney formula (Eq. (3.9)) gives two equations for in-plane averaged stresses in the homogenized layer, and the traction free condition (Eq. (3.12)) provides another equation for out-of-plane volume averaged stress. There are, however, six unknowns ($\left\langle \sigma^l_{\alpha\alpha} \right\rangle$ and $\langle \sigma^o_{\alpha\alpha} \rangle$ where $\alpha = x, y, z$). Therefore, three more equations are needed to calculate volume-averaged normal stresses in individual metal and dielectric lines. In the limit of high aspect ratio, the averaged strains on the $x-z$ plane for both lines should be the same (isostrain condition) [43], such that;

$$\frac{\left\langle \sigma^l_{xx} \right\rangle}{E_l} - \frac{\nu_l}{E_l} \left\langle \sigma^l_{yy} \right\rangle - \frac{\nu_l}{E_l} \left\langle \sigma^l_{zz} \right\rangle + \alpha_l \Delta T = \frac{\langle \sigma^o_{xx} \rangle}{E_o} - \frac{\nu_o}{E_o} \left\langle \sigma^o_{yy} \right\rangle - \frac{\nu_o}{E_o} \langle \sigma^o_{zz} \rangle + \alpha_o \Delta T. \tag{3.13}$$

$$-\frac{\nu_l}{E_l} \left\langle \sigma^l_{xx} \right\rangle - \frac{\nu_l}{E_l} \left\langle \sigma^l_{yy} \right\rangle + \frac{\left\langle \sigma^l_{zz} \right\rangle}{E_l} + \alpha_l \Delta T = -\frac{\nu_o}{E_o} \langle \sigma^o_{xx} \rangle - \frac{\nu_o}{E_o} \left\langle \sigma^o_{yy} \right\rangle + \frac{\langle \sigma^o_{zz} \rangle}{E_o} + \alpha_o \Delta T. \tag{3.14}$$

In this limit, equilibrium consideration shows that the averaged stresses in the y direction for both lines must be equal (isostress condition) [17], which leads to,

$$\left\langle \sigma^l_{yy} \right\rangle = \left\langle \sigma^o_{yy} \right\rangle. \tag{3.15}$$

Equations from (3.10) through (3.15), along with the Stoney formula (Eq. (3.9)), can be written in matrix form and solved explicitly. The volume-averaged stresses in the metal and dielectric lines can be computed from the following matrix

equation:

$$\begin{bmatrix} f_l & 0 & 0 & f_o & 0 & 0 \\ 0 & f_l & 0 & 0 & f_o & 0 \\ 0 & 0 & f_l & 0 & 0 & f_o \\ \frac{1}{E_l} & -\frac{\nu_l}{E_l} & -\frac{\nu_l}{E_l} & -\frac{1}{E_o} & \frac{\nu_o}{E_o} & \frac{\nu_o}{E_o} \\ -\frac{\nu_l}{E_l} & -\frac{\nu_l}{E_l} & \frac{1}{E_l} & \frac{\nu_o}{E_o} & \frac{\nu_o}{E_o} & -\frac{1}{E_o} \\ 0 & 1 & 0 & 0 & -1 & 0 \end{bmatrix} \begin{bmatrix} \langle \sigma_{xx}^l \rangle \\ \langle \sigma_{yy}^l \rangle \\ \langle \sigma_{zz}^l \rangle \\ \langle \sigma_{xx}^o \rangle \\ \langle \sigma_{yy}^o \rangle \\ \langle \sigma_{zz}^o \rangle \end{bmatrix} = \begin{bmatrix} -\Gamma(\kappa_x + \nu_s \kappa_y) \\ -\Gamma(\nu_s \kappa_x + \kappa_y) \\ 0 \\ \alpha_o - \alpha_l \\ \alpha_o - \alpha_l \\ 0 \end{bmatrix} \Delta T, \quad (3.16)$$

where $\Gamma = \frac{1}{6} \frac{h_s^2}{h} \frac{E_s}{1-\nu_s^2}$.

Since this is for the limiting conditions, *i. e.* a very high aspect ratio, this model does not account for the effect of line aspect ratio. In addition, at high aspect ratio, each line is contacted in a very limited region with a passivation layer which is deposited during the post process. Therefore, the model does not account for the effect of a passivation layer. As integration of semiconductor devices increases, however, line aspect ratio is getting higher, which makes this theory more practical for calculation of volume-averaged stresses in interconnect lines.

3.2.2 Multi-level structure

The evolution of curvatures of a multi-level structure can also be assessed using the above model by invoking the concept of superposition. Fig. 3-3 shows a schematic of two trilayer structures with different metal line arrangements on the upper level. One is an aligned structure with lines on the upper level running in the same direction as those on the lower level (Fig. 3-3(a)). The other is a perpendicular structure with lines on the upper level running in a perpendicular direction (Fig. 3-3(b)), which is a more realistic line arrangement in the semiconductor interconnect design. In the high aspect ratio limit, each structure can be regarded as the superposition of two composite layers, with an inter-level dielectric layer (ILD) between them. For a given

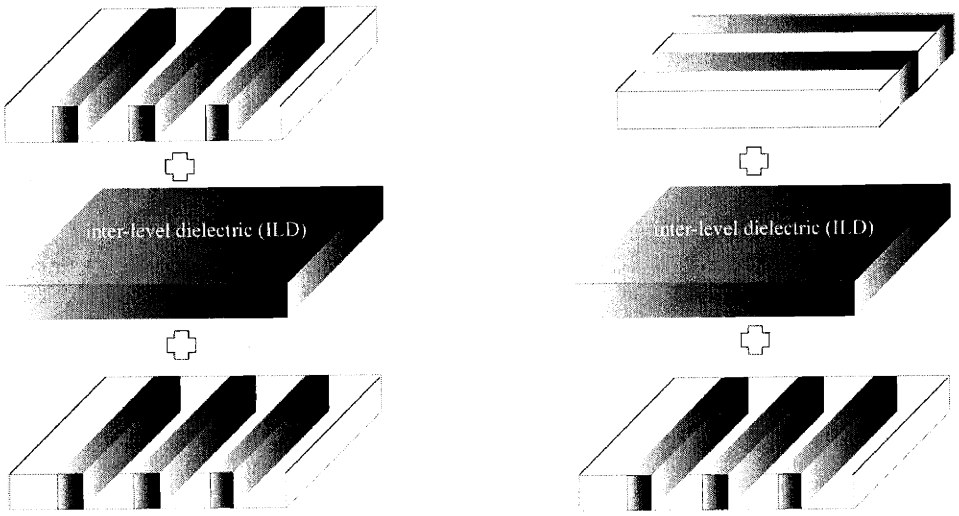

Figure 3-3: Superimposition of individual metal and ILD layers resulting in a tri-layer structure after a Dual Damascene process; (a) aligned structure (b) perpendicular structure.

ILD material, the curvature change resulting from the ILD layer, $\kappa_{\rm p}$, is obtained in terms of the biaxial modulus of the ILD layer, $\overline{E_{\rm p}}$ $(= E_{\rm p}/[1-\nu_{\rm p}])$, its thermal expansion coefficient, $\alpha_{\rm p}$, and its thickness, $h_{\rm p}$, as,

$$\kappa_{\rm p} = \frac{6}{\overline{E_{\rm s}}} \frac{h_{\rm p}}{h_{\rm s}^2} \overline{E_{\rm p}} (\alpha_{\rm p} - \alpha_{\rm s}) \Delta T. \tag{3.17}$$

By adding $\kappa_{\rm p}$ from the ILD layer (Eq. (3.17)) to κ_x's and κ_y's from two composite layers (Eqs. (3.7) and (3.8)) respectively, curvature changes of this trilayer structure, $\kappa_x^{'}$ and $\kappa_y^{'}$, are obtained:

$$\kappa_x^{'} = \kappa_x(\text{lower layer}) + \kappa_{\rm p}(\text{ILD layer}) + \kappa_{\rm x}(\text{upper layer}). \tag{3.18}$$

$$\kappa_y^{'} = \kappa_y(\text{lower layer}) + \kappa_{\rm p}(\text{ILD layer}) + \kappa_{\rm x}(\text{upper layer}). \tag{3.19}$$

The structure shown in Fig. 3-3 can be obtained by the Dual Damascene process [45]. It may be followed by additional processes such as another passivation layer

Table 3.1: Material properties used in the simulations.

	E (GPa)	ν	α (10^{-6} / °C)
Si	130	0.28	2.60
Cu	110	0.30	17.0
SiO_2	71.4	0.16	0.524
Si_3N_4	380	0.20	2.25

deposition and further metalization. The concept of superposition can be applied to the structure with more than 3 layers provided that linear elastic conditions are maintained.

3.3 Finite Element Method

The finite element method (FEM) was used to verify the present analytical model. For this purpose, the finite element program ABAQUS [63] was employed. Table 3.1 shows the material properties used in the simulations [39, 44]. In this work Cu and SiO_2 were chosen as the metal and dielectric materials, respectively, in light of the shift from conventional Al-based interconnects to new Cu Damascene structures in the semiconductor industry. Isotropic material properties were used and residual stresses, which may result from Cu deposition and/or polishing, were not taken into account. This analysis deals only with elasticity, which is expected to be valid over a wide range of practical interest since the material surrounding the Cu lines, especially in the case of passivated lines, leads to elevated levels of hydrostatic stress in the lines, thereby inducing constrained deformation [35].

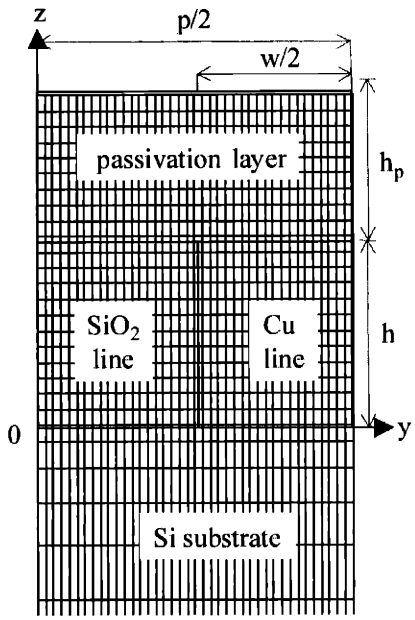

Figure 3-4: A representative unit cell (top portion) and finite element discretization for Cu lines with SiO_2 on the single layer for the 2-D generalized plane strain model.

3.3.1 2-D generalized plane strain model

A unit cell illustrating the mesh used in the 2-D numerical simulation is shown in Fig. 3-4. Due to the periodicity and symmetry of the arrangement, only a unit segment ranging from a symmetric axis and the neighboring periodic boundary is needed. Here h, w and p represent the height, width, and pitch of Cu lines, respectively. At the reference point marked "0" ($y = 0, z = 0$) in Fig. 3-4, the displacements along the y and z directions are taken to be zero. Along the symmetric axis ($y = 0$), the displacement in the y direction vanishes. This means

$$u_y = 0 \qquad at \;\; y = 0. \tag{3.20}$$

The outer boundary of the unit cell ($y = p/2$) is free to move, but it is forced

to remain a straight line. This gives

$$y = C_1 z + C_2 \qquad at \;\; y = \frac{p}{2}, \tag{3.21}$$

where C_1 and C_2 are constants to be determined with further analysis. No other boundaries are constrained during deformation. The wafer curvature across the lines (in the y-direction) can then be directly calculated from the relative positions of the representative points on the boundary, $y = p/2$;

$$\kappa_y = \frac{2}{h_s p}\{[u_y]_{y=\frac{p}{2},z=0} - [u_y]_{y=\frac{p}{2},z=-h_s}\}, \tag{3.22}$$

where h_s is the thickness of the substrate.

A generalized plane strain formulation, which is an extension of the plane strain framework (with the $y-z$ plane being the plane of deformation), is used in the calculations [38, 39]. This is done by superimposing a longitudinal strain, ϵ_{xx}, on the plane strain state. To properly simulate the actual response of the patterned parallel lines on the substrate, the strain field ϵ_{xx} is constrained to induce a constant rotation about the y axis,

$$\frac{\partial^2 u_z}{\partial x^2} = C_3, \tag{3.23}$$

where C_3 is a constant directly determined by the analysis. The three-dimensional effect can thus be adequately described by the present model. It gives the wafer curvature in the x direction:

$$\kappa_x = -\frac{\partial^2 u_z}{\partial x^2}. \tag{3.24}$$

The generalized plane strain model is thus capable of yielding more realistic field quantities in both phases than the strict plane strain formulation.

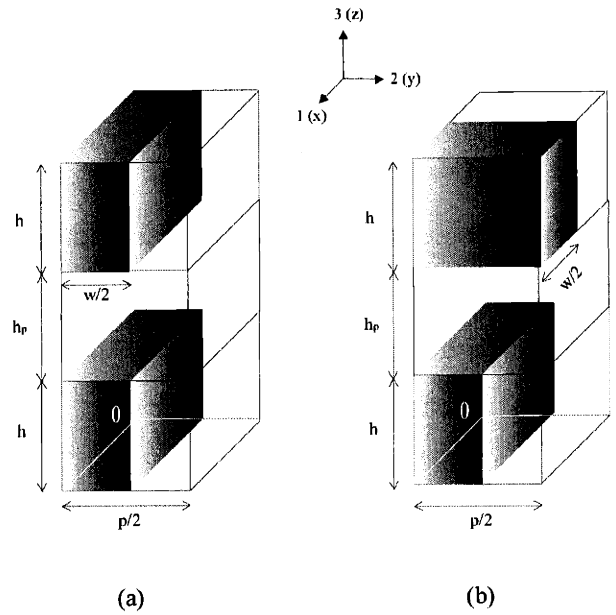

Figure 3-5: Representative unit cells (top portion) for 3-D finite element model for Cu lines with SiO_2 on the two level structure after Dual Damascene process; (a) aligned structure (b) perpendicular structure.

3.3.2 3-D model

Representative unit cells with different line arrangements on upper levels used in the 3-D numerical simulation are shown in Fig. 3-5. For the same reason as the 2-D simulation, the periodicity and symmetry enables us to use only a unit segment ranging from symmetric planes to the neighboring periodic boundaries for calculation. At the reference point marked "0" ($x = y = z = 0$), the displacements in all the directions are assigned to be zero. On one symmetric plane ($x = 0$), the displacement in the x-direction vanishes. On the other symmetric plane ($y = 0$), all the nodes are fixed in the y-direction.

The outer boundaries of the unit cells ($x = l$ and $y = p/2$) are free to move, but they are forced to remain as flat planes. This can be obtained by contacting frictionless, rigid surfaces on the outer boundaries. The curvature in the x-direction can then be calculated from the relative positions of the representative points on the

boundary , $x = l$;

$$\kappa_x = \frac{1}{h_s l}\{[u_x]_{x=l,y=\frac{p}{4},z=0} - [u_x]_{x=l,y=\frac{p}{4},z=-h_s}\}. \tag{3.25}$$

Similarly, the curvature in the y-direction is obtained from the relative positions of the representative points on the other boundary, $y = p/2$;

$$\kappa_y = \frac{2}{h_s p}\{[u_y]_{x=\frac{l}{2},y=\frac{p}{2},z=0} - [u_y]_{x=\frac{l}{2},y=\frac{p}{2},z=-h_s}\}, \tag{3.26}$$

In order to confirm the validity of the 3-D FEM, the results from passivated lines on the single-level structure were compared to those from the 2-D generalized plane strain model. The values for the stress distribution, as well as volume-averaged stresses and wafer curvature, were the same in both cases. Therefore, it is possible to use 3-D FEM for multi-level structure as an extension of 2-D FEM for single-level structure.

3.4 Results and Discussion

3.4.1 Single-level structure

Here the current curvature and stress model will be compared with finite element analysis using a 2-D generalized plane strain model in various line geometries such as line aspect ratio (h/w), passivation ratio (h_p/h) with different capping materials to figure out validity of our simple analytical model and discuss reasons for discrepancies between theory and numerical results. Effects of metal density ($w/p = f_l$) will be also discussed. Comparison with available experimental data will be presented.

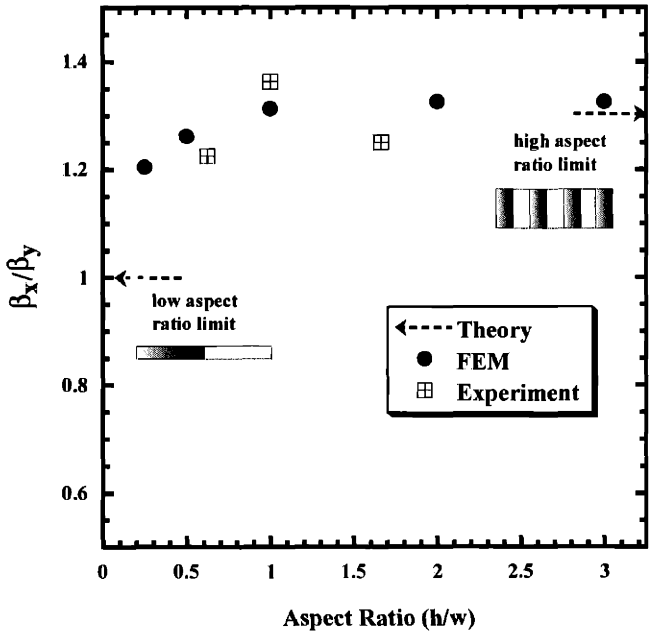

Figure 3-6: Ratios of thermal curvature coefficients between along (x) and across (y) line directions of single-level structure without passivation (w/p=f^d=0.5, $h = 1\mu m$ and $h_s = 525\mu m$) as a function of aspect ratio (h/w).

Curvature evolution as a function of line aspect ratios

Figure 3-6 shows ratios of thermal curvature coefficients ($\beta = \kappa/\Delta T$) between along and across lines as a function of aspect ratio, at a fixed pitch ratio ($p/w = 2$). At the low aspect ratio limit, the lines behave like individual Cu and oxide thin films. The curvatures in the x- and y- directions are therefore identical. At the high aspect ratio limit, it can be seen that the lines collectively compose a single composite layer with different effective thermoelastic properties, which results in anisotropic curvature values. FEM results are in good agreement with theoretical values at the high aspect ratio limit even down to h/w=1, then approach to the other theoretical limit as aspect ratios get lower. Although it is difficult to compare the current analysis to absolute experimental curvature values directly due to lack of exact thermoelastic property data in Cu and oxide lines in real specimens, comparison of the ratios between along and across the line directions would be useful. Curvature measurements of Damascene Cu lines on a Si substrate with different aspect ratios were previously reported [37]. These values are reasonably matched with the current analytical and numerical results, within experimental scatter, as shown in Fig. 3-6.

Effect of line and passivation geometry on stress evolution

Figure 3-7 illustrates the normal stress components during cooling from 200°C to room temperature (20°C) in Cu lines without passivation (capping) layer as a function of aspect ratio (h/w), at a fixed Cu density (f_l=0.5). At the low aspect ratio limit, Cu lines are so wide that they can be treated as thin Cu films. Therefore, an equibiaxial plane stress condition prevails, as shown from Eq. (3.1). FEM results deviate from the values expected from theory for the intermediate aspect ratios. However, as the aspect ratio increases, these results do approach the theoretical predictions, based on Eq. (3.16). This is due to the assumption of the current theory at high aspect ratio limit that individual Cu and SiO_2 lines are sufficiently tall such that the additional conditions in Eqs. (3.13)–(3.15) cna be used to calculate thermal stresses in each

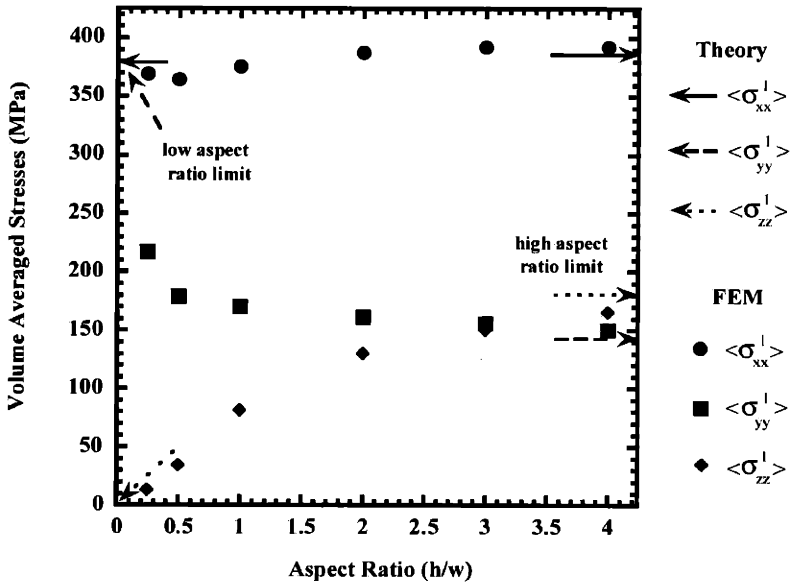

Figure 3-7: Volume-averaged stresses in Cu lines on single-level structures without passivation (w/p=f'=0.5, $h = 1\mu m$ and $h_s = 525\mu m$) as a function of aspect ratio (h/w) during cooling from 200°C to room temperature.

line. From Fig. 3-7 the theoretical values at the high aspect ratio limit underestimate $\langle \sigma'_{yy} \rangle$, and overestimate $\langle \sigma'_{zz} \rangle$ compared to FEM results at intermediate line aspect ratios. $\langle \sigma'_{xx} \rangle$ are well matched over a wide range of aspect ratios. The reason for these discrepancies between theory and FEM will be discussed later, along with the effects of a passivation layer.

The variation of normal stress component as a function of the thickness of the SiO_2 passivation layer are shown in Figs. 3-8 – 3-10. The $\langle \sigma'_{xx} \rangle$ values are not heavily influenced by passivation and correlate quite well with the theory as shown in Fig. 3-8. Values of $\langle \sigma'_{yy} \rangle$, however, increase with passivation, which leads to a more pronounced deviation in intermediate aspect ratios from the theoretical predictions at high aspect ratio limit (Fig. 3-9). Values of $\langle \sigma'_{zz} \rangle$ also increase when passivated, resulting in better agreement in intermediate aspect ratios with theoretical predictions at the high aspect ratio limit (Fig. 3-10). For both $\langle \sigma'_{yy} \rangle$ and $\langle \sigma'_{zz} \rangle$, there is little difference when the thickness of the passivation layer increases by a factor of 5.

Figure 3-11 shows contours of σ_{yy} in a Cu line and an oxide trench at various

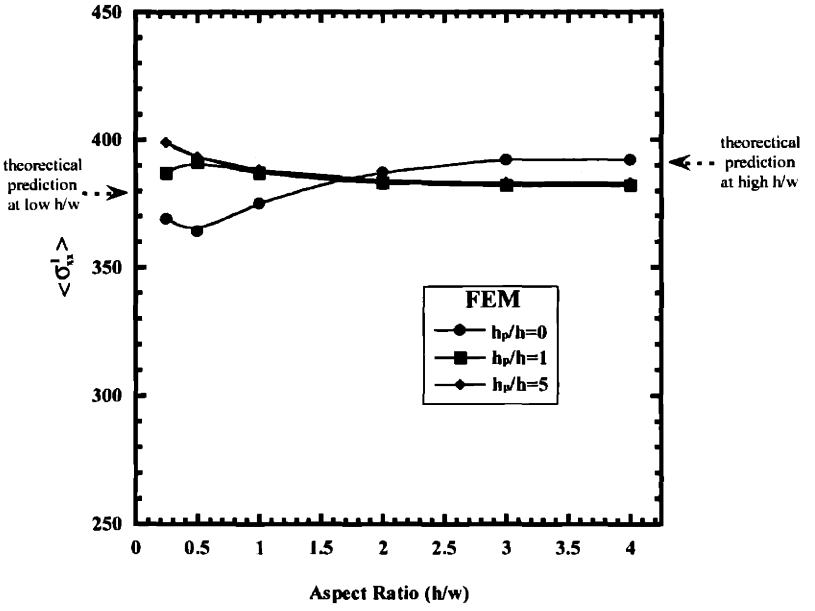

Figure 3-8: Volume-averaged stresses in Cu lines, $\left\langle \sigma_{xx}^{l} \right\rangle$, on single-level structures with various passivation thicknesses (w/p=f'=0.5, $h = 1\mu m$ and $h_s = 525\mu m$) as a function of aspect ratio (h/w) during cooling from 200°C to room temperature.

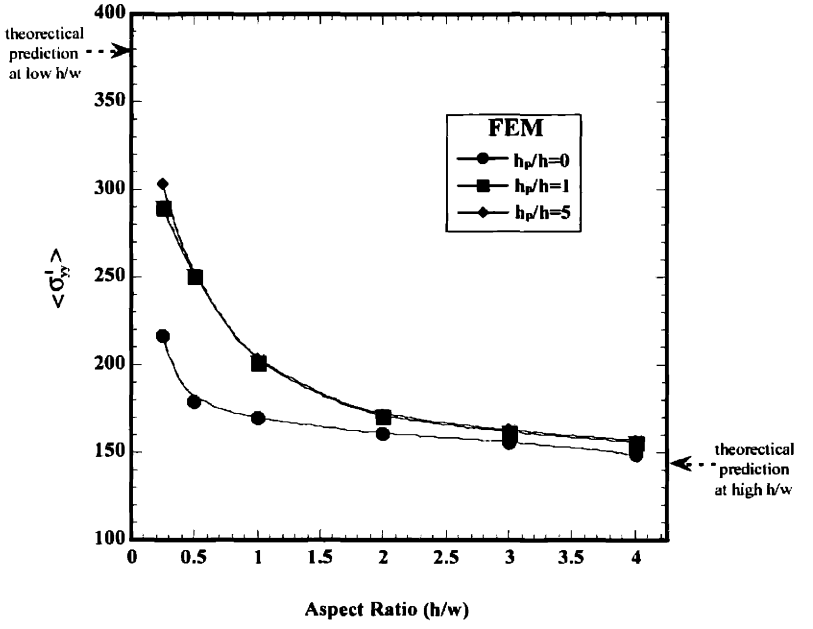

Figure 3-9: Volume-averaged stresses in Cu lines, $\left\langle \sigma_{yy}^{l} \right\rangle$, on single-level structures with various passivation thicknesses (w/p=f'=0.5, $h = 1\mu m$ and $h_s = 525\mu m$) as a function of aspect ratio (h/w) during cooling from 200°C to room temperature.

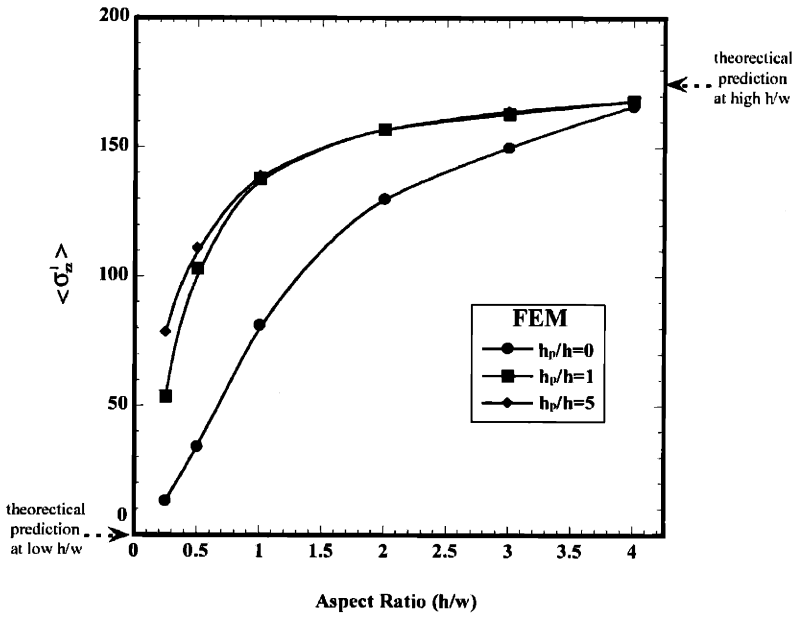

Figure 3-10: Volume-averaged stresses in Cu lines, $\langle \sigma_{zz}^{l} \rangle$, on single-level structures with various passivation thicknesses (w/p=f^{l}=0.5, $h = 1\mu m$ and $h_s = 525\mu m$) as a function of aspect ratio (h/w) during cooling from 200°C to room temperature.

aspect ratios and fixed metal density (f$_l$=0.5) when passivated with a SiO_2 layer (h_p/h=1). At h/w=1, the Cu line generally shows a higher stress than the oxide trench. When lines are taller (h/w=2), isostress condition across lines, Eq. (3.15), seems valid in the middle of lines and the FEM values in this region are quite well matched with the theoretical prediction from Eq. (3.16). Near interfaces between underlying/overlying (passivation) layers, however, deviation resulting from thermal mismatch will appear. Since SiO_2 was used for the overlying layer in this case, localized stresses in the Cu line near an interface are higher than stress values in the middle of the line. Localized stresses in the oxide trench are smaller than the stresses in the middle because the trench and overlying layer are composed of the same material, resulting in essentially no thermal mismatch between them. Alternatively, higher localized stress between the Cu line and the underlying Si substrate results from larger thermal mismatch between the Cu line/Si substrate. In the y-direction, $\langle \sigma_{yy} \rangle$, in the Cu and oxide lines near the interfaces are expected to nearly cancel out with each other. This is why the volume-averaged stresses of Cu lines in the y-direction, $\langle \sigma_{yy}^{l} \rangle$, exhibit higher values than theory (Fig. 3-9). However, curvature

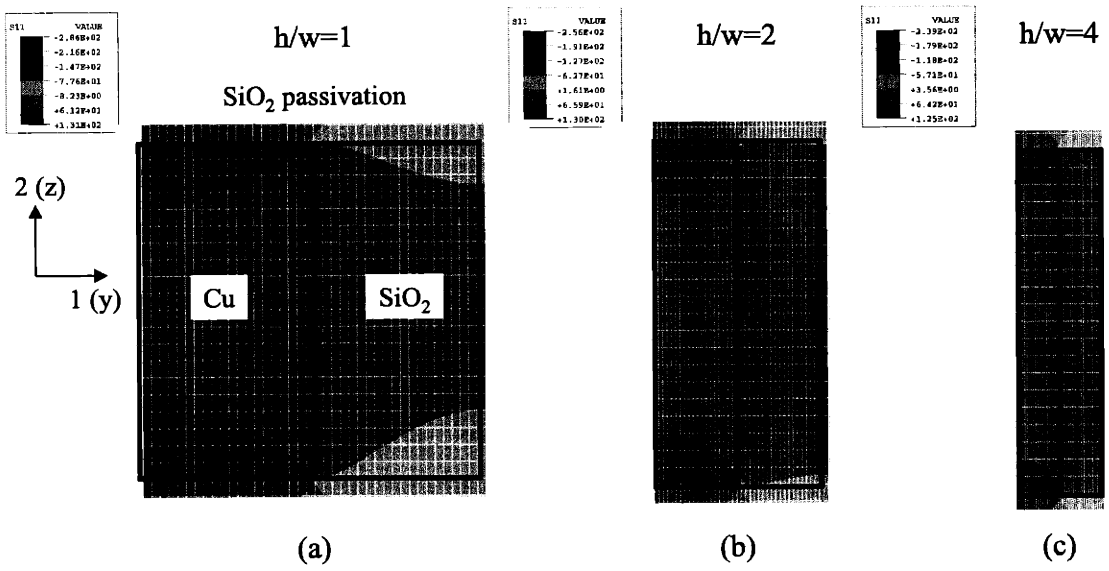

Figure 3-11: 2-D FEM contours of stress across lines, σ_{yy}, on single-level structures with SiO_2 passivation layers ($h = 1\mu m$, $h_p = 1\mu m$ and $h_s = 525\mu m$) at different aspect ratios during heating from room temperature to 200°C; (a) h/w=1 (b) h/w=2 (c) h/w=4.

values across the lines from the homogenized composite layer, κ_y, which are related to the volume averaged stresses of the overall layer, $\langle\sigma_{yy}\rangle$, with contributions from both Cu and oxide lines, show good agreement with theory even down to around h/w=1 (Fig. 3-7) [46]. When the aspect ratio is much higher (h/w=4), the areas of the region where localized stresses are found to be smaller, which may explain why FEM results approach theoretical prediction with aspect ratio.

Effect of passivation materials

Table 3.2 compares each volume-averaged normal stress component in the Cu lines passivated with either a SiO_2 or a Si_3N_4 layer. In addition to an increase in $\langle\sigma^l_{yy}\rangle$, there is a large increase in $\langle\sigma^l_{zz}\rangle$ when passivated with a Si_3N_4 layer. At the high aspect ratio limit, isostress conditions in the y-direction and isostrain conditions in the z-direction are assumed. When passivated with a capping layer, isostress conditions across the lines shows deviation resulting from localized stress near the interface

Table 3.2: Comparison of theoretical predictions of volume-averaged stresses in Cu lines on single-level structures without passivation and with SiO_2 or Si_3N_4 passivation to finite element results (w/p=f'=0.5, h/w=2, h_p/h=1, $h = 1\mu m$ and $h_s = 525\mu m$) during cooling from 200°C to room temperature (differences from theory shown in the parentheses)

	$< \sigma^l_{xx} >$ [MPa]	$< \sigma^l_{yy} >$ [MPa]	$< \sigma^l_{zz} >$ [MPa]	$< \sigma^l_h >$ [MPa]
Theory	377	146	180	234
FEM (unpass.)	387 (3%)	161 (10%)	130 (-27%)	226 (-3%)
FEM (SiO_2)	383 (2%)	171 (17%)	157 (-13%)	237 (1%)
FEM (Si_3N_4)	389 (3%)	179 (23%)	169 (-6%)	245 (5%)

between the lines and the passivation layer. Passivation, however, causes favorable effects on isostrain conditions out-of-plane. These effects in both the y- and z-directions become more pronounced when a stiffer capping layer is deposited.

Figure 3-12(a) shows a contour of σ_{zz} in a Cu line and an oxide trench (h/w=2 and f_l=0.5) when passivated with a SiO_2 layer (h_p/h=1). Near the interfaces between under/overlying layers, an isostrain condition in the z-direction, Eq. (3.14), does not work well since Cu is likely to have a higher strain than the oxide due to the much higher thermal expansion coefficient of Cu, relative to SiO_2, even when the lines are passivated with capping materials. The current theory assumes that the strains in the z-direction should be the same, which results in very stiff confinement of the Cu lines in the direction normal to the substrate because Cu tends to expand more than oxide. This leads to an overestimation of volume-averaged stresses of the Cu lines in the z-direction, $\langle \sigma^l_{zz} \rangle$, compared to FEM results (Fig. 3-10). Fig. 3-12(b) shows a contour of σ_{zz} when passivated with Si_3N_4. Because of its higher stiffness, it confines the Cu

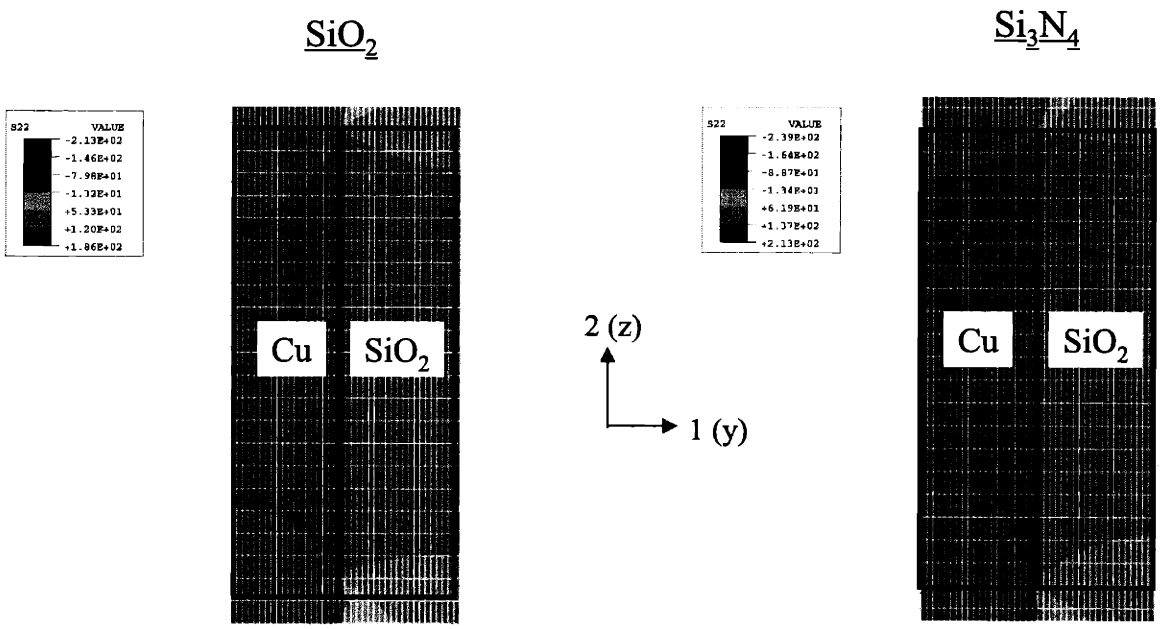

Figure 3-12: 2-D FEM contours of stress normal to the substrate, σ_{zz}, on single-level structures with different passivation layers (h/w=2, h_p/h=1, $h = 1\mu m$ and $h_s = 525\mu m$) during heating from room temperature to 200°C; (a) SiO_2 passivation (b) Si_3N_4 passivation.

lines in the z-direction more than the SiO_2 passivation layer. Therefore, it leads to an increase in $\left\langle \sigma_{zz}^{l} \right\rangle$, and the value becomes closer to the theoretical prediction.

- **Effect of thermoelastic properties of low k dielectrics**

Based on the analytical solution in this work, volume-averaged thermal stresses in copper interconnect lines and dielectric lines can be computed for lines that are sufficiently tall. Since most low k dielectrics replacing oxides are polymer-based materials, the relavant elastic constants are typically low. Hydrostatic stresses in lines in a wide range of thermoelastic properties of low k dielectics during cooling from 200°C to room temperature are shown in Fig. 3-13 and 3-14. Assuming Poisson's ratios of dielctics and the oxide are the same, while they are insensitive to the coefficients of thermal expansion (CTE) of the dielectrics, the thermal stresses in the Cu lines shown in Fig. 3-13 increase with higher dielectrics stiffness, which is in agreement

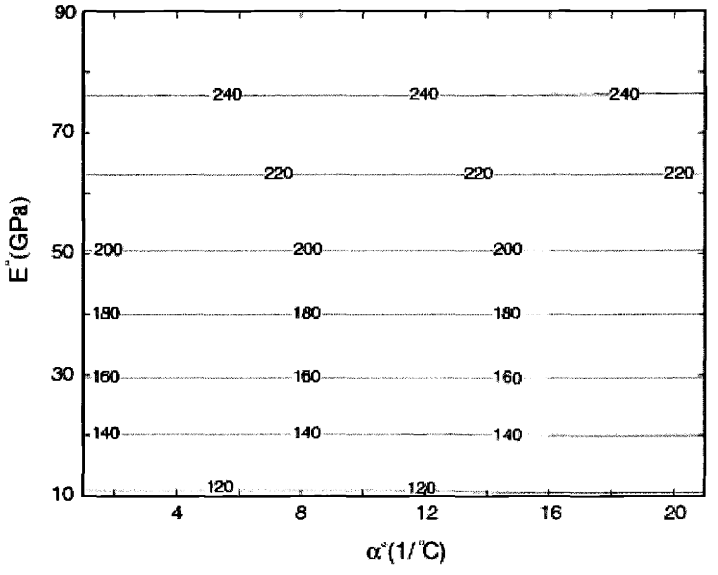

Figure 3-13: Analytical predictions of volume-averaged hydrostatic stresses as a function of thermoelastic properties of dielectric materials during cooling from 200°C to room temperature in Cu lines.

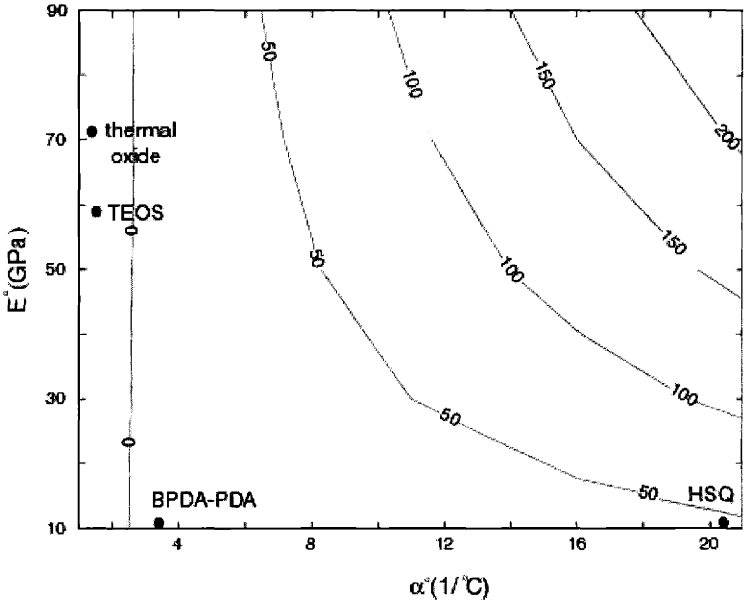

Figure 3-14: Analytical predictions of volume-averaged hydrostatic stresses as a function of thermoelastic properties of dielectric materials during cooling from 200°C to room temperature in dielectric lines.

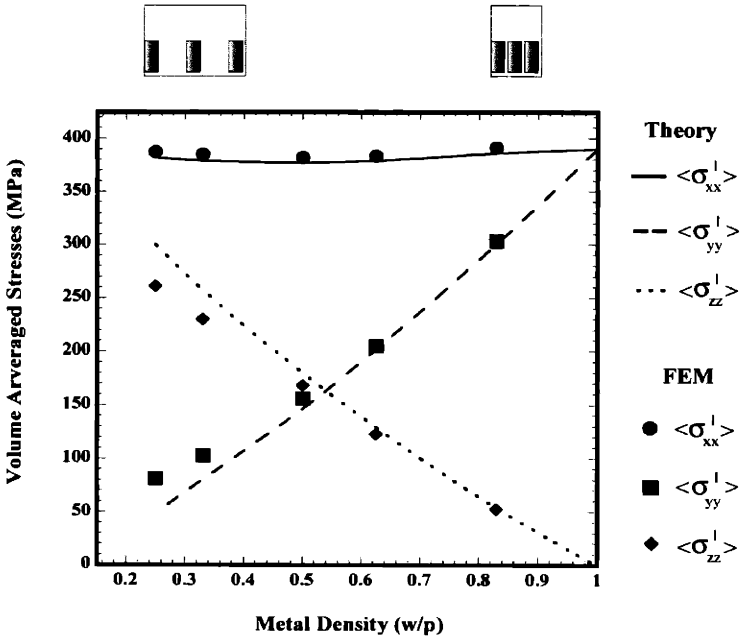

Figure 3-15: Volume-averaged stresses in Cu lines on single-level structures with SiO_2 passivation layer (h/w=4, h_p/h=1, $h = 1\mu m$ and $h_s = 525\mu m$) as a function of metal density (w/p) during cooling from 200°C to room temperature.

with previous finite element results [64]. Stresses in dielectrics (Fig. 3-14), however, depend on both thermoelastic properties. Corresponding stresses from some candidates for low k dielectrics [65] are indicated to illustrate how this map can be used for selection of dielectric materials in integration with Cu interconnects. Either of the high modulus / low CTE material (TEOS) or low modulus / high CTE material (HSQ) is compatible with Cu lines, as far as the thermal stress problem is concerned.

Effect of metal density

Figure 3-15 shows thermal stresses in Cu lines at a fixed line aspect ratio (h/w=4) with SiO_2 passivation (h_p/h=1). Lines with high aspect ratio were taken because we can minimize the effects of localized stresses from under/overlying layers. The validity of the theory at high aspect ratios can then be evaluated explicitly over a wide range of metal density. $\langle \sigma'_{xx} \rangle$ remains nearly constant with metal density. As metal density increases, however, $\langle \sigma'_{yy} \rangle$ increases and $\langle \sigma'_{zz} \rangle$ decreases. As the line

structure approaches a continuous Cu film (w/p=1), an equibiaxial stress condition ($\langle\sigma^l_{xx}\rangle$=$\langle\sigma^l_{yy}\rangle$) with plane stress ($\langle\sigma^l_{zz}\rangle$=0) is obtained. The current model is in good agreement with FEM results, especially when the spacing between lines is small. It does, however, show deviation from FEM values as the spacing becomes larger, since oxide lines no longer have high aspect ratios. The ability to predict the effect of metal density at a fixed aspect ratio is one of the advantages of the current model over the Eshelby-type inclusion theory which is unable to take into account the presence of neighboring lines [41, 42]. The stress model for passivated metal lines proposed by Wikström *et al* [43], however, produced very similar values as the model in the current work, over a wide range of metal density. Although their model cannot predict curvature evolution, the assumption that in-plane deformation in lines are totally controlled by substrate deformation seems good as far as volume-averaged stresses are concerned.

Comparison with experiments

Table 3.3 compares theoretical predictions of normal stress components in Cu lines with numerical simulation results and X-ray diffraction data. Since the line aspect ratio of this sample is not exceedingly high (h/w=0.7), it is difficult to compare directly with the theoretical prediction at high aspect ratio limit. The theory's underestimation of $\langle\sigma^l_{yy}\rangle$ and overestimation of $\langle\sigma^l_{zz}\rangle$ compared to FEM values have been discussed previously in an earlier section. Hydrostatic stress, however, which is usually taken to be a key parameter for electromigration simulation, [31] is quite well predicted. Finite element results capture the trend of stress values from X-ray measurement in spite of complicated line geometry, especially mixed passivation layers of SiO_2 and Si_3N_4. The differences between FEM and experimental results are due to inelastic deformation, such as plastic yielding and/or creep in the lines and the anisotropic material properties of Cu, which are not considered in this analysis.

Table 3.3: Comparison of theoretical predictions of volume-averaged stresses in Cu lines (with $0.1\mu m$ Si_3N_4 and $0.8\mu m$ SiO_2) to results of finite element analysis and X-ray diffraction experiments (w/p=f=0.5, h/w=0.7, h_p/h=1.3, $h = 0.7\mu m$ and $h_s = 525\mu m$) during cooling from 390°C to room temperature.

	$< \sigma^l_{xx} >$ [MPa]	$< \sigma^l_{yy} >$ [MPa]	$< \sigma^l_{zz} >$ [MPa]	$< \sigma^l_h >$ [MPa]
Theory	806	297	380	494
FEM	727	431	273	477
Experiment	539	459	222	407

3.4.2 Multi-level structure

In order to capture three dimensional (3-D) features of the multi-level structure, especially the perpendicular arrangement, 3-D finite element analysis was performed. Results will be analyzed to determine whether the curvature predictions are valid for the multi-level structure and to find how thermal stresses vary from level to level. The effect of upper level line arrangement on lower levels will be also discussed. It will then be shown whether analytical prediction of thermal stresses based on the theory in the limiting line geometry on the single layer can be applied to the stress estimation in the multi-level structure.

Calculation of curvatures using superimposition

Table 3.4 compares theoretical curvature predictions with 3-D FEM results in two different line arrangements following the Dual Damascene process shown in Fig. 3. In this calculation, both lower and upper levels have the same line structure (h/w=1 and f_l=0.5). In the aligned structure (Table 3.4(a)), the superimposition of three layers, *i. e.* two composite layers with lines running in the same direction and one ILD layer between them, provides very good agreements with FEM values. In the perpendicular structure (Table 3.4(b)), the same curvature values are expected in the

Table 3.4: Comparison of theoretical predictions of curvature changes of tri-layer structures (Fig. 3-3) after the Dual Damascene process to finite element results (w/p=f'=0.5, h/w=1, $h_p = 1\mu m$, $h = 1\mu m$ and $h_s = 525\mu m$) during heating from room temperature to 200°C; aligned and perpendicular structure

	Aligned		Perpendicular	
	κ_x (1/m)	κ_y (1/m)	κ_x (1/m)	κ_y (1/m)
Theory	0.0394	0.0293	0.0343	0.0343
FEM	0.0408 (+3.6%)	0.0297 (+1.2%)	0.0355 (+3.5%)	0.0352 (+2.6%)

x- and y-directions according to the theory due to the symmetric geometry. This is confirmed by numerical simulation.

Because of the high diffusivity of Cu through SiO_2 and Si, a diffusion barrier such as TaN is commonly employed [45]. Although this complicates the interconnect structures, the effect of this additional layer can easily be incorporated in the present model by superimposition for linear elasticity condition and may be negligible if this layer is very thin, *i. e.* on the order of a few hundred Å.

Effect of line arrangement on stress evolution on lower/upper levels

Figure 3-16 shows contours of hydrostatic stresses during cooling from 200°C to room temperature (20°C) in a two-level Cu interconnect structure without a passivation layer on the top of the upper level. This corresponds to the structure after polishing the excess Cu layer on the upper level in the Dual Damascene process. In this calculation, both lower and upper levels have the same line structure (h/w=1 and f_l=0.5). For the purpose of comparison, a hydrostatic stress contour of a single-level structure with passivation layer is shown in Fig. 3-16(a). In the aligned structure (Fig. 3-16(b)), the stress values in the Cu line on the upper level are much lower than those

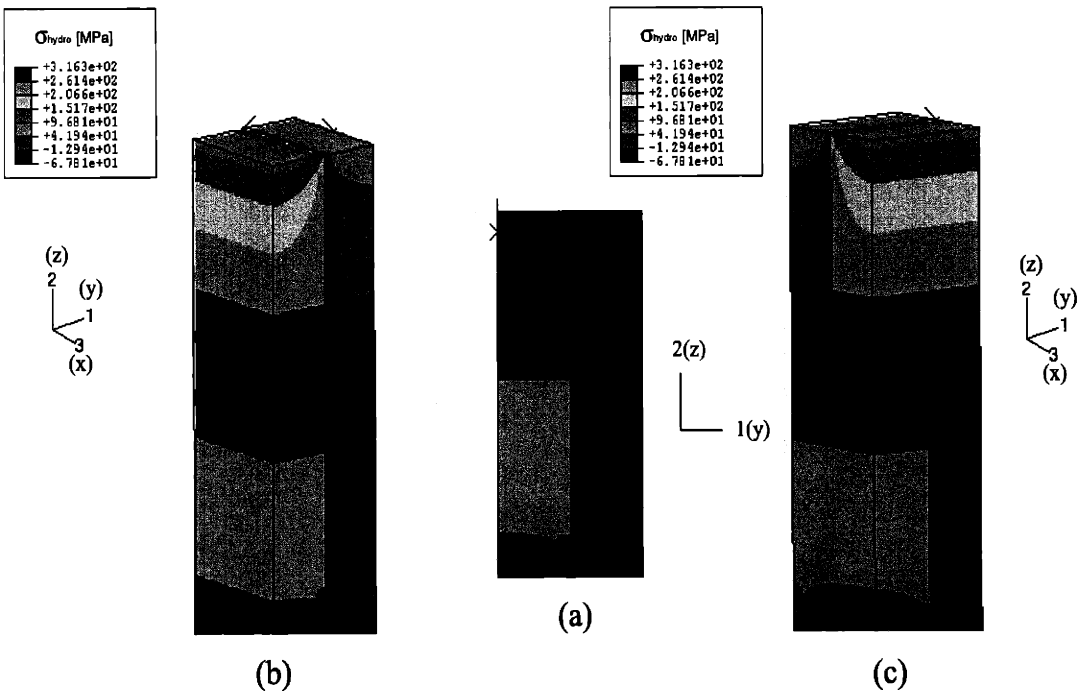

Figure 3-16: Contours of hydrostatic stress, σ_{hydro}, during cooling from 200°C to room temperature (h/w=1, h_p/h=1, $h = 1\mu m$ and $h_s = 525\mu m$); (a) single-level with SiO_2 passivation using 2-D FEM (b) two-level aligned structure and (c) two-level perpendicular structure after Dual Damascene process using 3-D FEM.

on the lower level. There are two main reasons for the above phenomenon. First, the lines on the upper level are farther from the stiff Si substrate, which relieves stresses, especially in the direction normal to the substrate. In addition, there is no passivation layer on the upper level of the structure after polishing. Therefore, based on the earlier argument, an absence of the passivation layer would reduce stress values in the Cu lines on the upper level. In the perpendicular structure (Fig. 3-16(c)), for the lines on the upper level almost the same results except direction, which seems 90° rotated, are shown compared to those in the aligned structure. Furthermore, hydrostatic stresses in the lines on the lower level are not heavily influenced by the presence and/or arrangement of the upper level.

Fig. 3-17 shows the contours of Mises stresses during cooling. Unlike hydrostatic stresses, Mises stresses are higher in the line on the upper level, except at sharp corner. This is due to the absence of the passivation layer on the upper level because

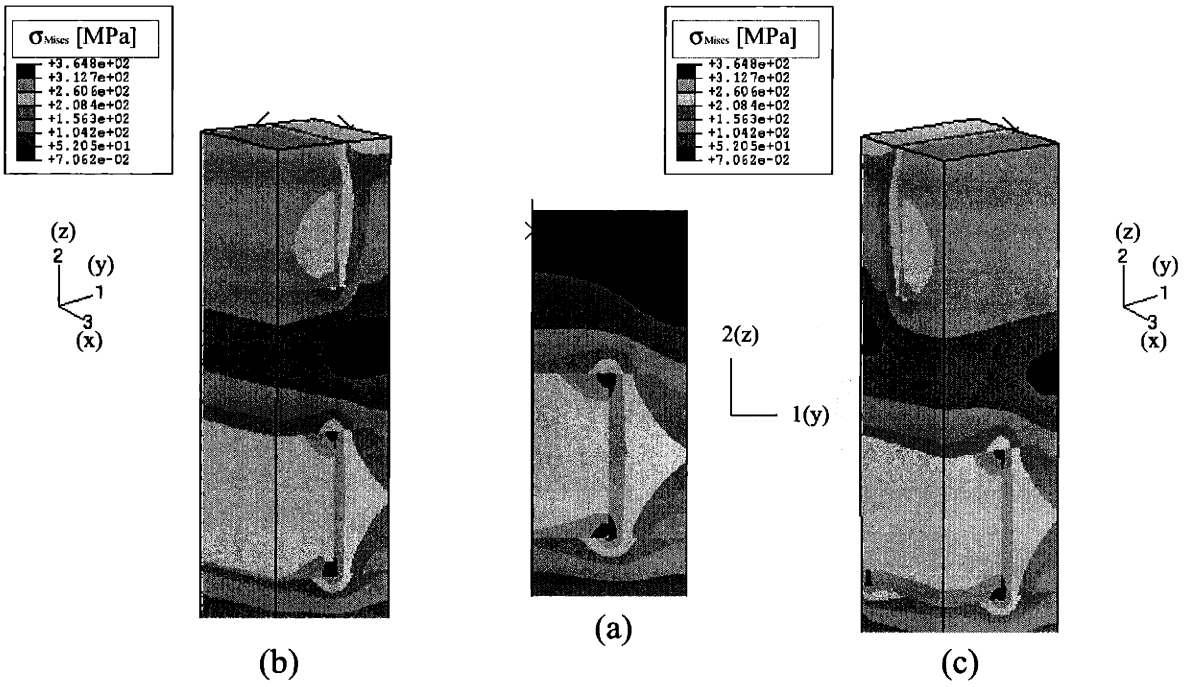

Figure 3-17: Contours of Mises stress, σ_{Mises}, during cooling from 200°C to room temperature (h/w=1, h_p/h=1, $h = 1\mu m$ and $h_s = 525\mu m$); (a) single-level with SiO_2 passivation using 2-D FEM (b) two-level aligned structure and (c) two-level perpendicular structure after Dual Damascene process using 3-D FEM.

unpassivated Cu lines which are in the trench with a free top surface may have high deviatoric components unless the aspect ratio is very high. It can also be seen that upper level lines show the same results in both the aligned and perpendicular arrangements, and lower level lines are hardly affected by the presence and/or arrangement of the upper level. It should be noted, however, that the difference of Mises stress distribution in the ILD layer can be found in different line arrangements. Typically, the stress values are not exceedingly high, but in general, new insulating materials with low dielectric constants have very low yield strength [33], which can influence other failure mechanisms, such as yielding in the dielectric.

For the structures in Fig. 3-16 and 3-17, volume-averaged values of each normal stress component, hydrostatic and Mises stresses are summarized in Table 3.5. Compared to a single-level structure, the stress components in the lower level lines of two-level structures basically remain unchanged, and are independent of the

Table 3.5: Comparison of volume-averaged stresses in Cu lines on single metal level structure with SiO_2 passivation and two metal level structures without passivation (w/p=f=0.5, h/w=1, $h_p = 1\mu m$, $h = 1\mu m$ and $h_s = 525\mu m$) during cooling from 200°C to room temperature.

		$< \sigma^l_{xx} >$ [MPa]	$< \sigma^l_{yy} >$ [MPa]	$< \sigma^l_{zz} >$ [MPa]	$< \sigma^l_h >$ [MPa]	$< \sigma^l_{Mises} >$ [MPa]
FEM (single)		387	202	138	242	239
FEM (double; align)	lower	386	200	139	242	237
	upper	375	170	81	209	280
FEM (double; perp.)	lower	386	199	138	241	236
	upper	373	171	80	208	281

Table 3.6: Comparison of volume-averaged stresses in Cu lines on single metal level structure with SiO_2 passivation and two metal level structures with passivation (w/p=f=0.5, h/w=1, $h_p = 1\mu m$, $h = 1\mu m$ and $h_s = 525\mu m$) during cooling from 200°C to room temperature.

		$< \sigma^l_{xx} >$ [MPa]	$< \sigma^l_{yy} >$ [MPa]	$< \sigma^l_{zz} >$ [MPa]	$< \sigma^l_h >$ [MPa]	$< \sigma^l_{Mises} >$ [MPa]
FEM (single)		387	202	138	242	239
FEM (double; align)	lower	386	199	139	242	237
	upper	383	198	131	237	236
FEM (double; perp.)	lower	385	200	141	241	236
	upper	375	197	130	234	238

arrangement of upper level lines. In the upper lines, however, $\langle \sigma_{yy}^{l} \rangle$ and $\langle \sigma_{zz}^{l} \rangle$ are smaller than those in the lower level lines. To separate effects of relative positions of the lines (whether lines lie on the lower or upper level) from effects of line geometry (whether lines are passivated or not), SiO_2 of the same thickness as the ILD layer was used for the passivation layer on the upper level (Table 3.6). The upper level stress values are nearly identical along and across the lines (in-plane stress components) as the lower one, but give slightly smaller values in the stress normal to the substrate (out-of-plane stress component). This is in an agreement with a previous result from Shen [66]. This can result from the fact that the upper level lines are closer to the free surface, so the constraint imposed by the surrounding oxide is not as strong as that experienced by the lower level lines. There is little difference between the aligned and perpendicular line arrangements. Therefore, it can be seen that interaction between levels in the vertical direction is quite weak when the thickness of inter-level dielectric (ILD) becomes comparable to that of metal layer, which is commonly found in practical multilevel structures in the semiconductor industry.

Extension to four-level structure

The finite element analysis of volume-averaged stresses can be extended to a four-level structure with the same line geometry (h/w=1, h_p/h=1 and f_l=0.5) as seen in Table 3.7. It is clear that the difference from level two to level four in the stress components is negligible. Since Si is much stiffer than SiO_2, the deformation of Cu on the lower level is more constrained than that on the upper level. As long as line aspect ratios are sufficiently low or high, this implies that the current theoretical preditions of stress evolution based on the limiting line geometry in the single-level structure are applicable to any level of a multi-level structure, with a slight difference in the out-of-plane stress in the first level on the substrate.

Table 3.7: Comparison of volume-averaged stresses in Cu lines on each level from a four-level structure (w/p=f^l=0.5, h/w=1, $h_p = 1\mu m$, $h = 1\mu m$ and $h_s = 525\mu m$) during cooling from 200°C to room temperature.

	$< \sigma^l_{xx} >$ [MPa]	$< \sigma^l_{yy} >$ [MPa]	$< \sigma^l_{zz} >$ [MPa]	$< \sigma^l_h >$ [MPa]
FEM (M1)	384	199	139	241
FEM (M2)	381	196	132	236
FEM (M3)	381	196	132	236
FEM (M4)	381	196	131	235

3.5 Conclusions

On the basis of theoretical and numerical analyses carried out in the present work for the single- and multi-level interconnect line structure, the following conclusions are made:

- The interconnect structure comprising metal and dielectric lines can be characterized by two limiting cases. In the limit of very low aspect ratios, each metal and dielectric line behaves like an individual thin film, and equibiaxial plane stress conditions prevail in each line. When lines are sufficiently tall, the line structure is homogenized into a single composite layer with different effective thermoelastic properties along and across the lines due to geometrical anisotropy. The 2-D finite element method using a generalized plane strain model is in good agreement with theoretical predictions as the line geometry approaches the limiting cases and also shows a gradual transition at intermediate line aspect ratios.

- When passivated with a capping layer, an isostress condition across the lines shows deviation resulting from localized stresses near the interface between the lines and passivation layer. Passivation, however, causes favorable effects on the isostrain out-of-plane condition. These effects in both the y- and z-directions become more pronounced as the stiffness of the capping layer increases.

- The current stress model can predict the effect of metal density at a fixed aspect ratio. This is one of the advantages over the Eshelby-type inclusion theory which is unable to take into account presence of neighboring lines. It can be shown that interaction between lines on the same level, *i. e.* in the lateral direction, is sufficiently strong that it cannot be neglected.

- Comparison of the current model to available experimental data shows reasonable agreement, considering the complicated line geometry and the inelastic deformation/anisotropic material propertes in the sample which this analysis does not take into account.

- From 3-D FEM results of the two-level structure, there is little difference between the aligned and perpendicular line arrangements. Therefore, it can be seen that the interaction between levels in the vertical direction is quite weak when the thickness of the inter-level dielectric (ILD) layer becomes comparable to that of the metal layer.

- In a multi-level structure, the difference between the stress components in the second level through the top layer is negligible. This implies that the current theoretical predictions of stress evolution in the single-level structure are applicable to any level of the multi-level structure, with a slight difference in the out-of-plane stress on the first level as long as line geometry approaches the limiting cases.

Chapter 4

Experiments on Large Deformation of Thin Film-Substrate Systems

Large deformation behavior prior to and after bifurcation of thin W films on much thicker Si substrates is investigated by recourse to coherent gradient sensing (CGS), which is an optical, full-field and vibration-insensitive technique. Since fringe patterns obtained by CGS indicate the out-of-plane displacement gradient through differentiation with appropriate optics, curvature of the wafer can be obtained directly from the fringe number density, a double differentiation of the displacement. The measured curvatures in two orthogonal principal directions, whose values agree reasonably with both analytical and numerical predictions based on large deformation theory, clearly show that the equilibrium shape of the wafer changes from a sphere to an ellipsoid when bifurcation occurs. In contrast to a one-dimensional scanning method, which provides only a normal curvature component, twist (shear) as well as normal components of curvatures near the center of the wafer can be obtained as the wafer is rotated with respect to a flat zone. A classical Mohr's circle representation has been used to rationalize evolution of twist curvatures. Finally, local curvature variation due to non-uniform film stresses can be captured by a full-field curvature map obtained through numerical differentiation of fringe patterns using image processing analysis.

4.1 Introduction

The drive for miniaturization and more efficient computer chip manufacturing has motivated the microelectronic industry to fabricate increasingly large Si wafers on which a greater number of dies could be fabricated. At the turn of the century, the semiconductor industry is in the midst of retooling its wafer fabrication facilities to handle 300-mm (12-inch) diameter Si wafers, instead of the current standard, 200-mm wafers. This increase in wafer diameter is also accompanied by a growing trend to introduce more levels of metallization on the Si substrate which, in turn, results in a higher effective membrane force in the multi-level, thin film arrangement on the substrate. Trends in the fabrication of copper metal interconnects using the Damascene process also involve the so-called chemical-mechanical polishing (CMP) method whereby planarization is achieved between different metallization steps. The collective effect of these trends in computer chip manufacturing is that while the propensity for inducing large deformation in the substrate is significantly enhanced, there is also growing need to ensure that wafer surfaces remain planar during different stages of manufacturing.

Dimensional analysis and computational modeling of large deformation indicate that the propensity for bifurcation is proportional to the mismatch stress in the film (σ_f), the film thickness (h_f) and the square of the substrate diameter (D_s^2), and inversely proportional to h_s^3, where h_s is the thickness of the substrate [48, 49, 50, 51, 52, 53, 54, 55]. These dimensional considerations for large deformation also suggest that for fixed substrate diameter, film mismatch stress and film thickness, there exists a critical thickness of the substrate above which curvature bifurcation is suppressed [53]. Similarly, different combinations of substrate geometry and film membrane force for which nonlinear elastic deformation is suppressed can also be identified [53]. When a wafer undergoes large deformation, curvatures are no longer uniform over the entire wafer even with uniform film membrane force. Non-uniform curvatures prevail from a center of the wafer to edges [53, 54] and are also

affected by gravity [55].

Large deformation and bifurcation have been observed with different curvature measurement techniques. Finot *et al.* [53] investigated thin W films on 6-inch and 8-inch diameter Si wafers, the backsides of which were polished to induce large deformation. Non-uniform curvature values were measured along the wafer diameter over a range of film membrane forces and substrate geometries with laser scanning method. The grid reflection technique, which projects a grid on the surface of wafers then collects a reflected image containing information on out-of-plane displacement of the surface, was also employed to capture bifurcation behavior [53].

Lee *et al.* [56] found nonlinear deformation in thin Al films on 2-inch diameter, ultra thin (105μm) Si wafers during thermal cycling using the coherent gradient sensing (CGS) technique, which obtains the out-of-plane displacement gradient of the surface. Techniques based on optical interferometry offer much promise as a means for real-time, non-intrusive, full field measurement of curvature changes. However, standard interferometric techniques, such as Twyman-Green interferometry, are sensitive to rigid body motion, and therefore are very vibration-sensitive. Moreover, since these interferrometric techniques measure the surface topography, two successive differentiations of the experimental data are required to obtain curvature. Since CGS technique measures gradient of displacements on the speciemen surface, this technique is vibration-insensitive and requires only one differentiation of the experiemental data to get curvature field.

In this work, twist (shear) curvature components as well as normal components of back-side polished, 6-inch Si wafers coated with thin W films, which are elastically isotropic, were measured using the CGS technique. Wafer and film thickness were varied to either promote or suppress bifurcation. Two orthogonal principal curvatures are compared with both analytical and numerical predictions based on large deformation theory. Fringe patterns were found to change as a function of wafer rotation, and classical Mohr's circle representation was used to rationalize normal

and twist curvature variation with rotation angles. Finally full-field curvature maps were constructed from CGS fringe patterns using an image processing technique for non-uniform curvature fields.

4.2 Theoretical Background

4.2.1 Curvature analysis based on large deformation theory

The curvature of a substrate coated with a thin film in an equibiaxial stress state is linearly proportional to the membrane force, $\sigma_f \times h_f$, by Stoney [13] as

$$\kappa_{Stoney} = \frac{6}{\overline{E_s}} \frac{\sigma_f h_f}{h_s^2}, \tag{4.1}$$

where $\overline{E_s}$ is the biaxial modulus ($E_s/[1-\nu_s]$) of the substrate. Since this relation is based on small deformation theory assuming small rotation, there is no dependence on lateral dimensions such as substrate diameter. When out-of-plane displacement is comparable to substrate thickness, large deformation theory, which accounts for moderate rotation, should be used to capture actual curvature changes of the thin film-substrate structure.

In order to evaluate quantitatively the significance of large deformation, it is convenient to introduce a stress parameter , A, defined [53] as

$$A = \sigma_f h_f \frac{D_s^2}{h_s^3}. \tag{4.2}$$

The parameter A, which primarily controls the extent of large deformation, also provides a geometrical interpretation in that it is proportional to the ratio of the out-of-plane deflection to the wafer thickness. It is known that bifurcation and geometrical instability of a circular wafer coated with a thin film occur at a critical value of the stress parameter, A_c [48, 49, 50, 51, 52]. For $D_s/h_s \geq 50$, A_c depends only on the

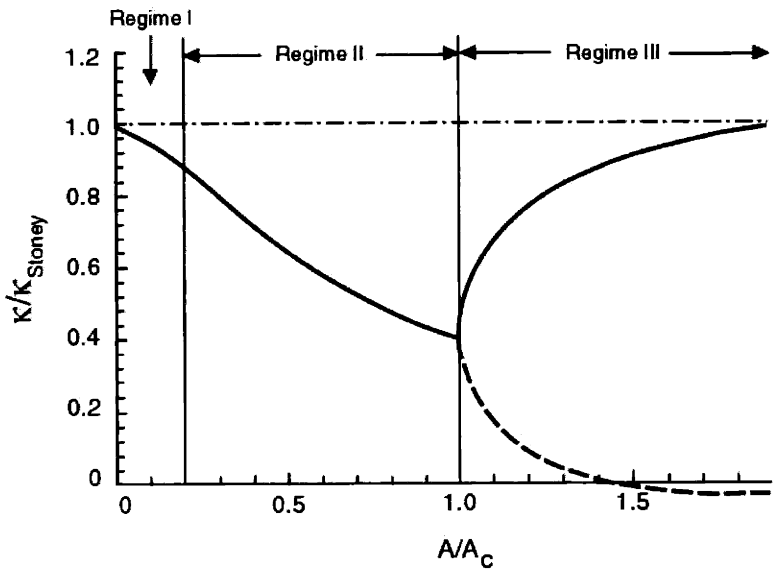

Figure 4-1: Numerical predictions of principal curvatures at wafer center normalized by the small deformation spherical curvature (κ_{Stoney}) as a function of the ratio A/A_c.

mechanical properties of the substrate, and full field finite element analysis gives A_c=680 GPa for a Si substrate [53].

Figure 4-1 shows the variation of curvature κ at the center of the wafer from numerical simulation, normalized by the predicted small deformation curvature κ_{Stoney}, as a function of the parameter A, normalized by its critical value A_c at bifurcation [53]. There are three distinct regimes which mark clear transitions in the evolution of curvature. For low values of A/A_c, the stresses in the film promote only small deformation with the result that the Stoney formula (Eq. (4.1)) adequately describes the evolution of the spherical curvature. Specifically when $A/A_c \leq 0.2$ (regime I), the curvature of the wafer predicted from the finite element analysis, κ, deviates by less than 10% from the small deformation approximation. In regime I, the curvature is uniform along the entire wafer.

When $0.2 \leq A/A_c \leq 1.0$ (regime II), the spherical shape of the film-substrate system is retained. The large deformation of the bilayer, however, leads to a non-linear relationship between the curvature, κ, and the membrane force, $\sigma_f \times h_f$. Consequently, the numerical values of κ deviate markedly from the Stoney prediction. In addition,

the curvature is not uniform across the wafer and the variation of the curvature between the center of the wafer and the edge is larger than 10%, even with uniform membrane force.

When the value of A approaches A_c, bifurcation occurs in the curvature of the film-substrate system, and the layered solid undergoes an abrupt shape change from a spherical geometry to an ellipsoidal shape. For $A/A_c \geq 1$ (regime III), this ellipsoidal shape leads to a large curvature, κ_x, in one direction and a smaller curvature, κ_y, in the in-plane orthogonal direction. As A/A_c increases, κ_y goes to zero and the wafer consequently becomes cylindrical.

4.2.2 Mohr's circle representation of curvature components

Similar to the state of stress in a body subjected to external forces, the curvature of a surface can be defined as a point and characterized as a tensor quantity. Consequently, the principal curvatures which represent the maximum and minimum values of curvature, the maximum twist (shear) curvature, and the principal curvature directions can be defined at each point on a curved surface.

Mohr's circle offers a convenient method to visualize the state of plane stress and to extract, from simple geometrical manipulations, normal and shear stresses and directions of principal stresses. Similarly, Mohr's circle can be constructed to define and determine different components of curvature at any point on a deformed surface. For displacements associated with the evolution of deformation at a point on a curved surface, the three components of curvature, κ_x, κ_y and κ_{xy}, can be generally nonlinear functions of the orthogonal displacements at the point and their derivatives with respect to the spatial coordinate; each of the three curvatures also depends on the orientation of the coordinate system with reference to the surface. For deformed surfaces where the slopes are small compared to unity, the three components

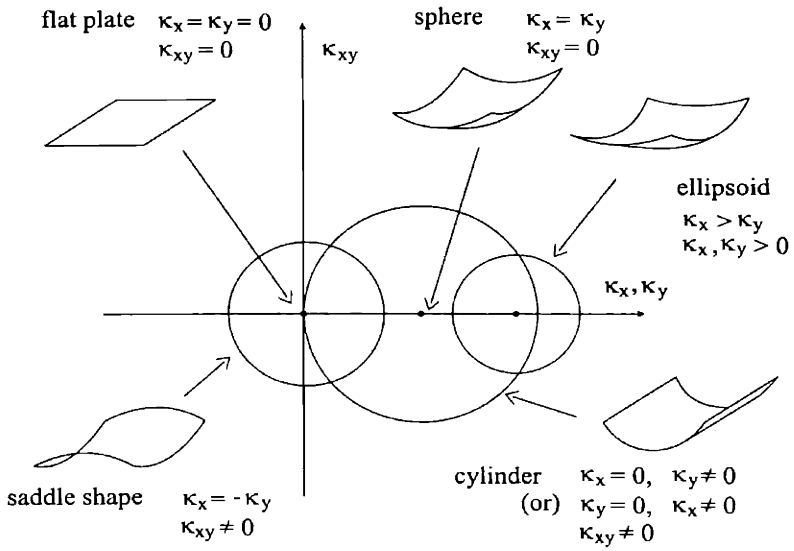

Figure 4-2: Mohr's circle representation of the shapes of curved surfaces.

of curvature can be defined in a simplified form as [67]

$$\kappa_x = \frac{\partial^2 f}{\partial x^2}, \kappa_y = \frac{\partial^2 f}{\partial y^2}, \kappa_{xy} = \frac{\partial^2 f}{\partial x \partial y}, \tag{4.3}$$

where $f(x, y)$ is out-of-plane displacement. The last equation defines the twist or shear curvature.

The Mohr's circle for curvature is drawn with κ_x and κ_y plotted as variables along the abscissa and κ_{xy} plotted along the ordinate, as shown in Fig. 4-2 [52, 67]. The center of the Mohr's circle, located along the abscissa at the value, C_{Mohr}, and its radius, R_{Mohr}, are given, respectively, by

$$C_{Mohr} = \frac{\kappa_x + \kappa_y}{2}, R_{Mohr} = \left\{ \left(\frac{\kappa_x - \kappa_y}{2} \right)^2 + \kappa_{xy}^2 \right\}^{1/2}. \tag{4.4}$$

The principal curvatures for the surface, representing the maximum and minimum values of normal curvature, are then simply given by

$$\kappa_1 = C_{Mohr} + R_{Mohr}, \kappa_2 = C_{Mohr} - R_{Mohr}. \tag{4.5}$$

The principal curvatures are found at directions θ and θ+90°, where

$$\tan 2\theta = \frac{2\kappa_{xy}}{\kappa_x - \kappa_y}. \tag{4.6}$$

In other words, θ is the angle through which the coordinate system should be rotated counterclockwise about the z-axis (looking toward the x-y plane along the z-direction) in order to align the x and y axes with the principal curvatures, κ_1 and κ_2. Mohr's circle can be used to determine which of these two axes is aligned with κ_1 or κ_2. Whereas the twist curvature vanishes in the principal curvature directions, maximum twist curvature κ_{12} occurs at orientations $\theta \pm 45°$ and is given by

$$\kappa_{12} = \frac{\kappa_1 - \kappa_2}{2} = R_{Mohr}. \tag{4.7}$$

Different shapes of curved surfaces are easily visualized using the Mohr's circle, as shown in Fig. 4-2. For a flat surface with no curvature, κ_x=κ_y=κ_{xy}=0, and the Mohr's circle reduces to a point located at the origin of the κ_x/κ_y versus κ_{xy} plot. For spherically curved surfaces, the Mohr's circle is a point located along the abscissa. For a cylindrical surface, either κ_x or κ_y vanishes and the Mohr's circle has its left or right extreme coincident with the origin of the curvature plot. For a saddle-shaped surface, the Mohr's circle encloses the origin.

4.3 Experiment and Analysis

4.3.1 CGS Interferometry

Two Si wafers with 150mm diameter, 675μm initial thickness, and (100) surface orientation were prepared for this study. In order to induce different extents of large deformation, the wafers were ground and polished from the back side. The effect of residual stress in the silicon due to grinding and polishing is known to be negligible

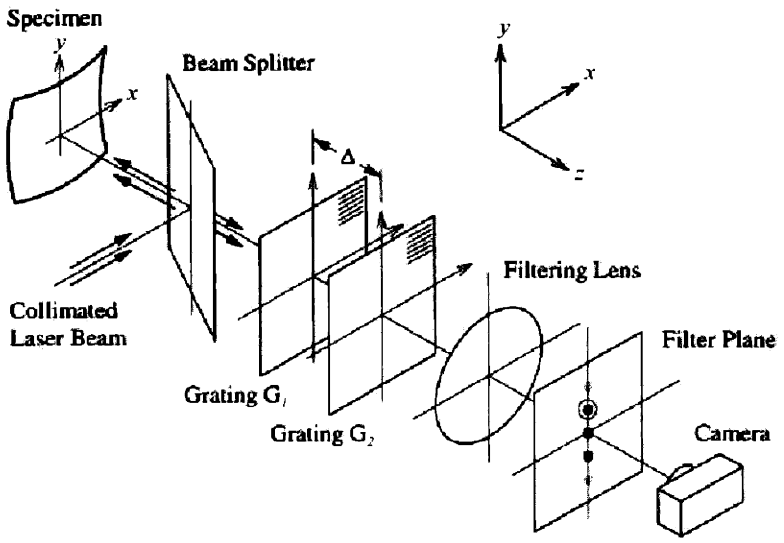

Figure 4-3: Schematic of the CGS set up in reflection mode.

[53]. The film-substrate geometries discussed here include a $325\mu m$ thick substrate with a $0.9\mu m$ thick W film (wafer A) and a $415\mu m$ thick substrate with a $2.4\mu m$ thick W film (wafer B). Curvatures were measured by CGS interferometry for both wafers and compared with the previous experimental results of identical specimens using the laser scanning and grid reflection methods [53]. Numerical simulation was forced to match the measured curvature (at the center region) to extract membrane force in the films from the fit. This membrane force was used to calculate κ_{Stoney} from Eq. (4.1).

Figure 4-3 shows a schematic of the CGS setup in reflection [56, 68]. A coherent, collimated laser beam is directed to the specularly reflecting specimen surface via a beam splitter. The beam reflected from the specimen then passes through the beam splitter and is then incident upon a pair of identical high-density (40 lines/mm) Ronchi gratings, G_1 and G_2, separated by a distance, Δ. The diffracted orders from the two gratings are spatially filtered using a filtering lens to form distinct diffraction spots on the filter plane. An aperture placed in this plane serves to filter out the diffraction order of interest, which is then imaged onto the photographic film plane. For our purpose, either of the ± 1 diffraction orders is of interest, as will be clear in the following discussion.

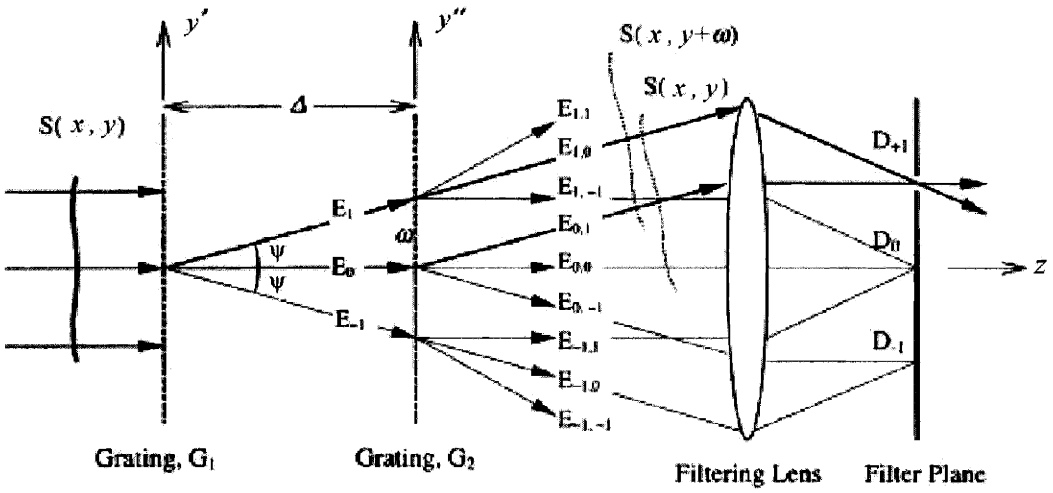

Figure 4-4: Schematic to illustrate the working principle of CGS.

Figure 4-4 illustrates the working principle of CGS in two dimensions [56]. Consider an optical wave front, $S(x, y)$, reflected from the specimen, which is directly related to out-of-plane displacement, $f(x, y)$, via the relation

$$S(x, y) = 2f(x, y) \tag{4.8}$$

A wave front incident on the primary grating, G_1, is diffracted into several wave fronts denoted as E_0, E_1, E_{-1}, E_2, E_{-2}, etc. For illustrative purposes, only E_0, E_1, E_{-1} are shown in Fig. 4. Each of these wave fronts are further diffracted by the second grating, G_2, to give rise to wave fronts denoted as $E_{0,0}$, $E_{0,1}$, $E_{0,-1}$, ..., $E_{1,0}$, $E_{1,1}$, $E_{1,-1}$, ...,$E_{-1,0}$, $E_{-1,1}$, $E_{-1,-1}$, etc. Again, only some of the diffracted wave fronts are shown. Now various sets of parallel diffracted beams are combined using the filtering lens to form diffraction spots D_0, D_1, D_{-1}, ... in the filter plane which coincides with the focal plane of the lens. An aperture is placed on the filter plane to block all but D_{+1} diffraction spot. Subsequently, this diffraction spot is imaged onto the film plane.

Assume that the optical wave front incident on the first grating, G_1, is approximately planar and has a local phase difference given as $S(x, y)$. Consider only two diffracted wave fronts, $E_{1,0}$ and $E_{0,1}$. For $E_{1,0}$, it is diffracted at the first grating and

transmitted without diffraction at the second. For $E_{0,1}$, it is transmitted at the first grating and is diffracted at the second. Since both wave fronts undergo one transmission and one diffraction, these wave fronts should be coherent, i.e. in the same phase. The net effect of the two gratings is to produce a lateral shift, or shearing, of the incident wave front. Thus the optical wave front along the diffracted beam $E_{1,0}$, given by $S(x, y+\omega)$, is shifted by an amount ω along the y-direction as compared to the wave front along the diffraced beam $E_{0,1}$, given by $S(x, y)$. The wave front shift is parallel to the principal axis of the gratings, i.e. along y-direction, if the grating lines are oriented along the x-direction as shown in Fig. 4-4.

Moreover, the magnitude of the shift is a function of the grating separation Δ and the diffraction angle ψ as

$$\omega = \Delta \tan \psi, \tag{4.9}$$

where the diffraction angle, ψ, is given by

$$\psi = \arcsin(\lambda/p), \tag{4.10}$$

with λ being the wavelength of light and p being the grating pitch. For a small angle of diffraction, Eqs. (4.9) and (4.10) approximate to

$$\omega \approx \Delta\psi, \tag{4.11}$$

$$\psi \approx \frac{\lambda}{p}. \tag{4.12}$$

Now consider the interference of the wave fronts. The conditions for constructive interference may be expressed as

$$S(x, y+\omega) - S(x, y) = n^{(y)}\lambda, n^{(y)} = 0, \pm 1, \pm 2, ... \tag{4.13}$$

where $n^{(y)}$ represents the integer identifying fringes observed for shearing along the

y-direction. Dividing Eq. (4.13) by ω gives

$$\frac{S(x,y+\omega)-S(x,y)}{\omega}=\frac{n^{(y)}\lambda}{\omega}, n^{(y)}=0,\pm1,\pm2,... \tag{4.14}$$

which, for sufficiently small ω, may be approximated by

$$\frac{\partial S(x,y)}{\partial y}=\frac{n^{(y)}\lambda}{\omega}, n^{(y)}=0,\pm1,\pm2,... \tag{4.15}$$

Using Eqs.(4.11) and (4.12) in Eq. (4.15), we have

$$\frac{\partial S(x,y)}{\partial y}=\frac{n^{(y)}p}{\Delta}, n^{(y)}=0,\pm1,\pm2,... \tag{4.16}$$

Generalizing the result to include wave front shearing in either the x- or y-direction, we have

$$\frac{\partial S(x,y)}{\partial y}=\frac{n^{(\alpha)}p}{\Delta}, n^{(\alpha)}=0,\pm1,\pm2,... \tag{4.17}$$

where n^{α} represents the fringes observed for shearing along the α-direction and $\alpha \in \{x,y\}$. Eq. (4.17) is the governing equation for interferograms formed using the technique of CGS.

$\kappa_{\alpha\beta}$, where $\alpha,\beta \in \{x,y\}$, is the symmetric curvature tensor whose components κ_{xx} (or κ_x) and κ_{yy} (or κ_y) are termed as the normal curvatures and κ_{xy} termed as the twist curvatures. The principal values of $\kappa_{\alpha\beta}$ are termed as the principal curvatures. When $(\nabla f)^2 < 1$, curvatures can be expressed combining Eq. (4.8) as

$$\kappa_{\alpha\beta}\approx\frac{\partial^2 f(x,y)}{\partial x\partial y}\approx\frac{p}{2\Delta}\left(\frac{\partial n^{(\alpha)}(x,y)}{\partial\beta}\right), n^{(\alpha)}=0,\pm1,\pm2,... \tag{4.18}$$

where $\alpha \in \{x,y\}$. Eq. (4.18) is the principal governing equation for determining curvature tensor fields, $\kappa_{\alpha\beta}(x,y)$, where $\alpha,\beta \in \{x,y\}$, from CGS interferograms. In this manner, CGS interferograms provide a full-field technique for determining the instantaneous value of the specimen curvature tensor at any point (x,y). Moreover, since CGS technique provides the out-of-plane gradient of the specimen surface topog-

raphy, it is not sensitive to rigid body motion such as vibration. In addition, only one differentiation of the experimemtal data is required to obtain curvature since the CGS interferogram is already differentiated once by optical means.

4.3.2 Image processing analysis

After obtaining the out-of-plane displacement gradient by CGS, numerical differentiation of the gradient field was computed via a commercial MATLAB program [69] to construct full-field curvature map. To improve the accuracy of fringe identification, the negative image of the CGS interferogram was used. As a result, fringe locations were identified as regions exceeding the threshold value of brightness. Pitch (or spacing) between two adjacent fringes was measured and its reciprocal value, directly related to local fringe density, was assigned to the corresponding region. Subsequent multiplication of the smoothed, inverse pitch map by $p/2\Delta$ provides full-field curvature map for enabling us to get information on non-uniform curvature and stress distribution. Detailed descriptions of image processing analysis will be given in Appendix.

4.4 Results and Discussion

4.4.1 Average curvatures compared to large deformation theory

Figure 4-5 shows CGS interferograms in two orthogonal principal directions. The view field is 2 inches in diameter in the central portion of the 6-inch (150mm) wafer. This limited field of view results mainly from the fact that the incident laser beam size does not cover the entire wafer, and beam splitters of 4 inches in diameter are inclined 45° with respect to the incident beam. It can be noted that, in general,

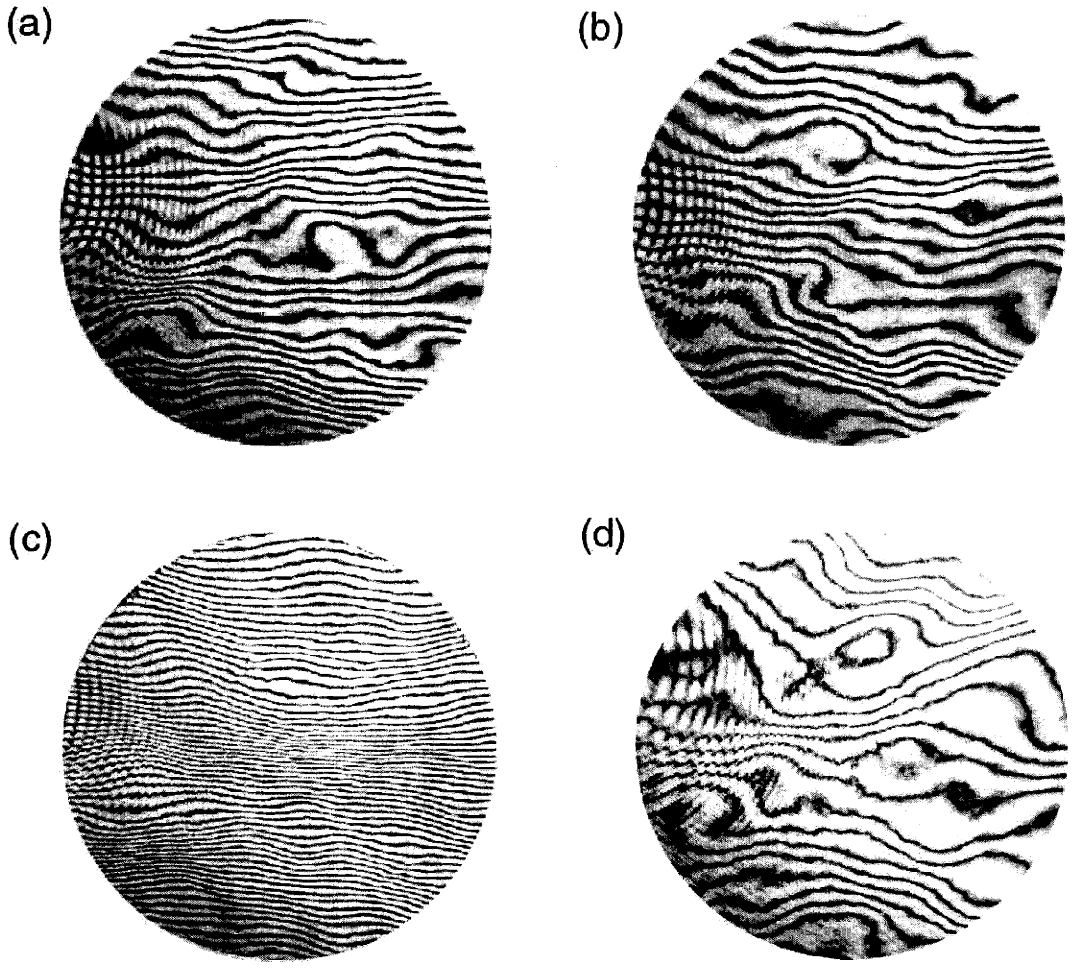

Figure 4-5: CGS interferrograms of two orthogonal principal directions before bifurcation, (a) and (b), and after bifurcation , (c) and (d), with view field diameter of 2-inch.

fringes are oriented horizontally (parallel to grating lines), which is indication of principal directions. Noises due to the incident laser beam is observed as fringe ripples in the outer regions, and can be removed via image processing. Average curvature over the region shown in Fig. 4-5 can be calculated from average fringe number density, i.e. total fringe number in the shown interferogram divided by the view field diameter. Variation in local fringe density, which is related to localized curvature, will be discussed in the following section. For wafer A (Fig. 4-5(a) and (b)), fringe patterns are approximately the same in two principal directions, which means the shape of this wafer remains spherical even in large deformation. For wafer B, however, the number of fringes is increased markedly compared to wafer A in one principal direction (Fig. 4-5(c)) while average fringe density is suppressed in the other direction (Fig. 4-5(d)). It can be thus observed that bifurcation occurs in wafer B, and the equilibrium shape changes into an ellipsoidal one.

Average principal curvatures, the values of which are calculated from the experimentally measured fringe number density and Eq. (4.18), are compared to predictions via large deformation theory [54] in Fig. 4-6. Additional experimental data from the literature, using laser scanning and grid reflection methods [53] are shown for comparison. Curvature and membrane force (or mismatch strain) are normalized into unitless values as below:

$$\bar{\kappa} = \frac{\kappa D^2}{16 h_s}, \tag{4.19}$$

$$\bar{\epsilon}_m = \frac{3\sigma_f h_f D^2}{8\overline{E_s} h_s^3}, \tag{4.20}$$

where $\overline{E_s}$ is 180 GPa for a (100) Si wafer. Agreement between the theory and the experimental measurements is reasonably good for both pre- and post-bifurcation curvatures in the central portion of Si wafers with W film deposits. The observed discrepancy may be due to non-uniform curvature evolution, which is not accounted for in theoretical predictions.

In addition to principal curvatures, normal and twist curvature components

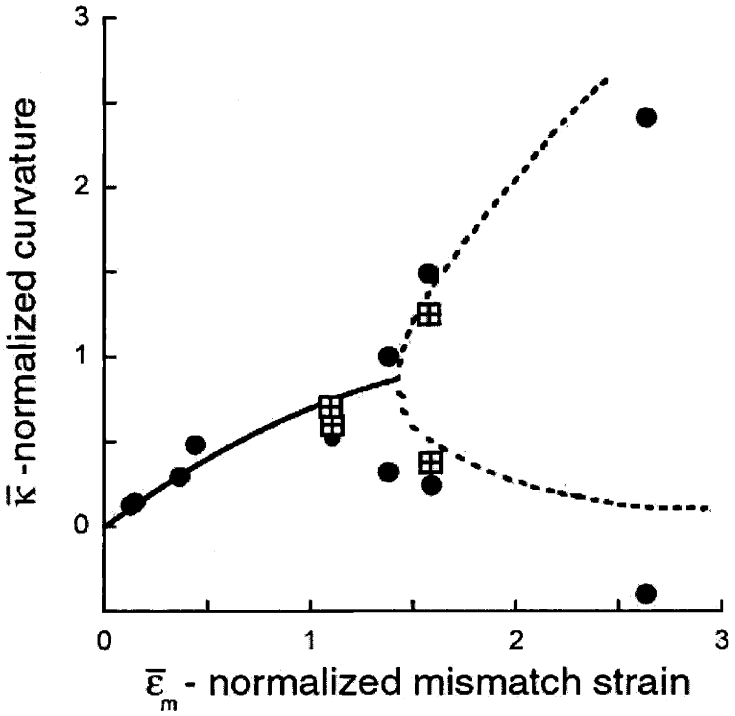

Figure 4-6: Comparison of measured normalized curvature versus normalized mismatch strain for Si wafers with W films to analytical prediction based on large deformation by Freund [54]. The filled circles correspond to curvature measurement made by Finot *et al.* [53], and the other window symbols denote experimental results from this work.

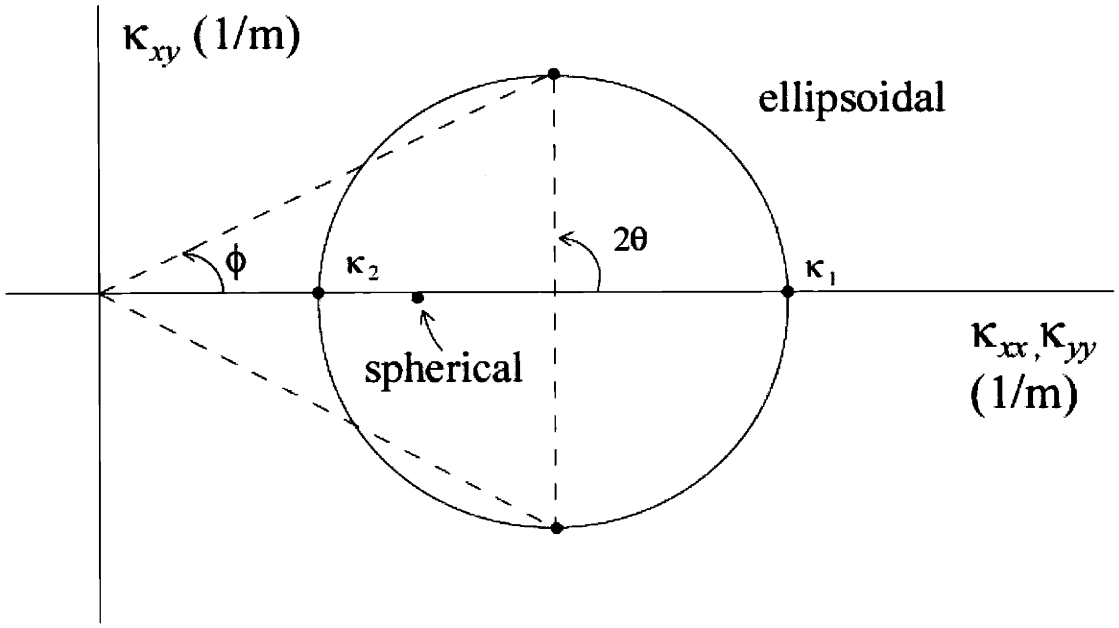

Figure 4-7: Schematic of Mohr's circles of spherical wafer shape (before bifurcation) and ellipsoidal shape (after bifurcation) to illustrate curvature components and characteristic angle, ϕ, as rotated by θ from principal direction.

can be identified at any arbitrary rotation angle θ with respect to principal directions from CGS interferograms. Fig. 4-7 shows the Mohr's circle representation for pre- and post-bifurcation. Prior to bifurcation (wafer A), a spherical shape is retained with essentially the same principal curvatures in two orthogonal directions. Therefore, Mohr's circle is reduced to a point located along the abscissa. After bifurcation (wafer B), however, one principal curvature is larger than that of the pre-bifurcated wafer, and the other is smaller. For an ellipsoidally curved surface, Mohr's circle is located with its center on the abscissa and its radius defined by Eq. (4.4). When a wafer is rotated counter-clockwise by θ from the principal direction, twist as well as normal curvature components are found at 2θ counter-clockwise from the abscissa. The angle ϕ, shown in Fig. 4-5, is defined by the ratio of twist component to normal curvature as

$$\phi = \arctan\left(\frac{\kappa_{xy}}{\kappa_{\alpha}}\right), \tag{4.21}$$

where α is either x or y.

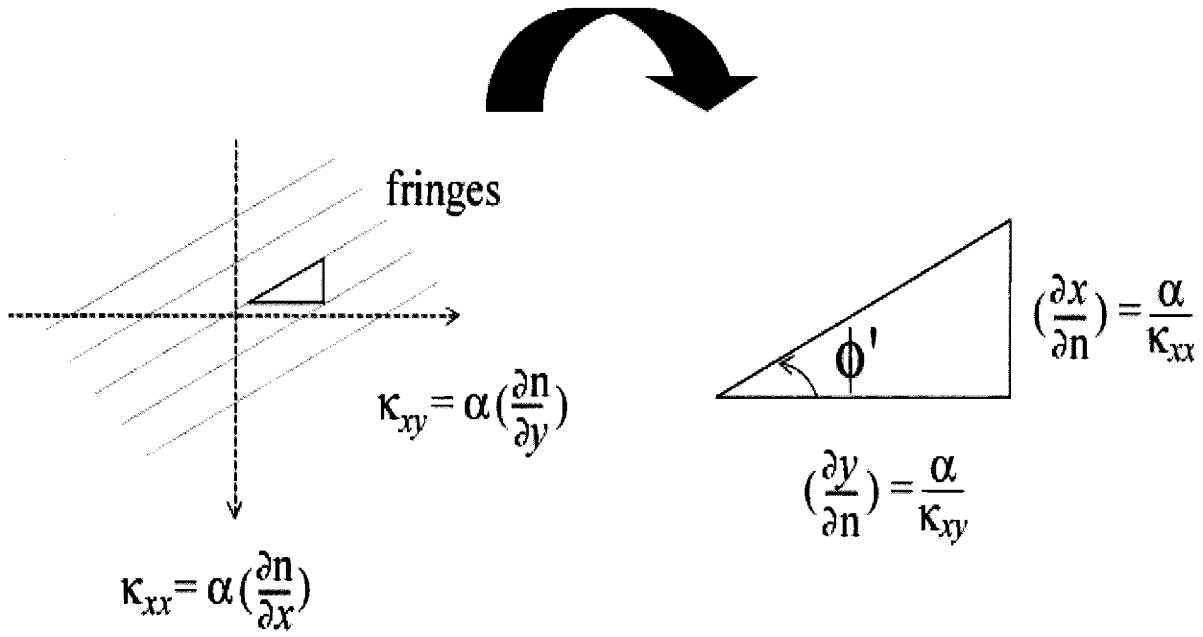

Figure 4-8: Schematic of CGS interferrogram as rotated by θ from principal direction (a) measurement of normal and twist curvature components (b) calculation of characteristic angle, ϕ'.

A schematic of the fringe pattern in an off-principal direction is shown in Fig. 4-8(a). Fringes are no longer parallel to grating lines (horizontal in this experiment), which means there are both normal and twist components of the curvature. The normal component, κ_y, is measured from the average fringe density along the y-direction. In the same way, average fringe density along the x-direction determines the twist component, κ_{xy}. It can be seen that the orientation of the fringes with respect to the grating lines represents the ratio of twist to normal curvature. As shown in Fig. 4-8(b), the angle ϕ' is defined in the same form as ϕ in Eq. (4.21). Therefore, predictions of κ_y (or κ_x), κ_{xy} and ϕ at a rotation angle of θ from Mohr's circle based on two principal curvature values, κ_1 and κ_2, can be compared to measurements from CGS interferograms.

Figure 4-9 shows CGS interferograms at θ=±45°, where maximum twist curvatures are expected. When the post-bifurcated wafer (wafer B) is rotated by 45° counter-clockwise (θ=+45°), fringes are oriented with a positive slope from left to right (Fig. 4-9(a)). In contrast, when the wafer is rotated by 45° clockwise (θ=–45°),

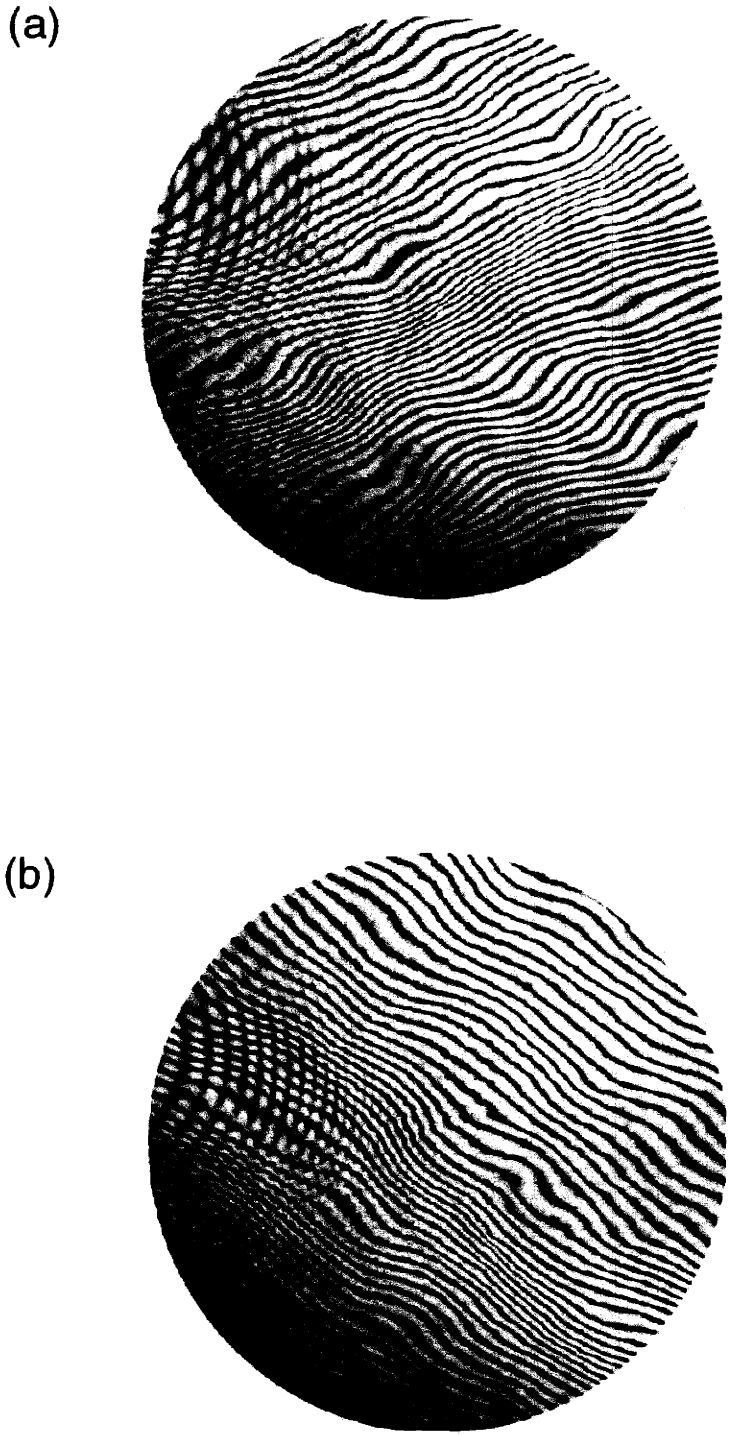

Figure 4-9: CGS interferrograms (a) θ=+45° (b) θ=–45°.

Table 4.1: Comparison between Mohr's circle predictions and CGS interferrogram results on normal, twist curvature components and characteristic angle, ϕ, at $\pm 45^{\circ}$ off principal directions.

	Mohr's circle	Interferogram	
		θ=+45°	θ= −45°
κ_x or κ_y (1/m)	0.24	0.27	0.23
κ_{xy} (1/m)	0.13	0.13	0.16
ϕ (°)	28	26	33

the fringe pattern is distorted in the same general manner but in the opposite sense, indicating the onset of substrate twist of opposite sign. Predictions of κ_y (or κ_x), κ_{xy} and ϕ at θ=$\pm$45° from Mohr's circle and measurements of corresponding values from CGS interferograms are listed in Table 4.1. Agreement between predictions and experiments for these in-plane orientations is reasonably good.

Curvature states are summarized on the Mohr's circle with corresponding CGS interferograms as a function of rotation angle for pre- and post-bifurcated wafers in Fig. 4-10. Prior to bifurcation, all the fringe patterns are essentially independent of rotation angle. In contrast, after bifurcation, fringe number increases in one principal direction and decreases in the other for fringes oriented parallel to the grating lines. At $\theta = \pm 45^{\circ}$, where the maximum twist curvatures occur, fringes have inclination to some degree in opposite sense depending on rotating direction. The numbers and inclination of fringes in these states can be predicted from Mohr's circle; Eq. (4.21) fringes at $\theta = \pm 45^{\circ}$ are approximately parallel to the dotted lines in the Mohr's circle shown in Fig. 4.10.

4.4.2 Localized curvatures in a full-field map

Figure 4-11 shows the center portion of a CGS interferogram for a post-bifurcated in the principal direction with smaller curvature (a) and the corresponding full field

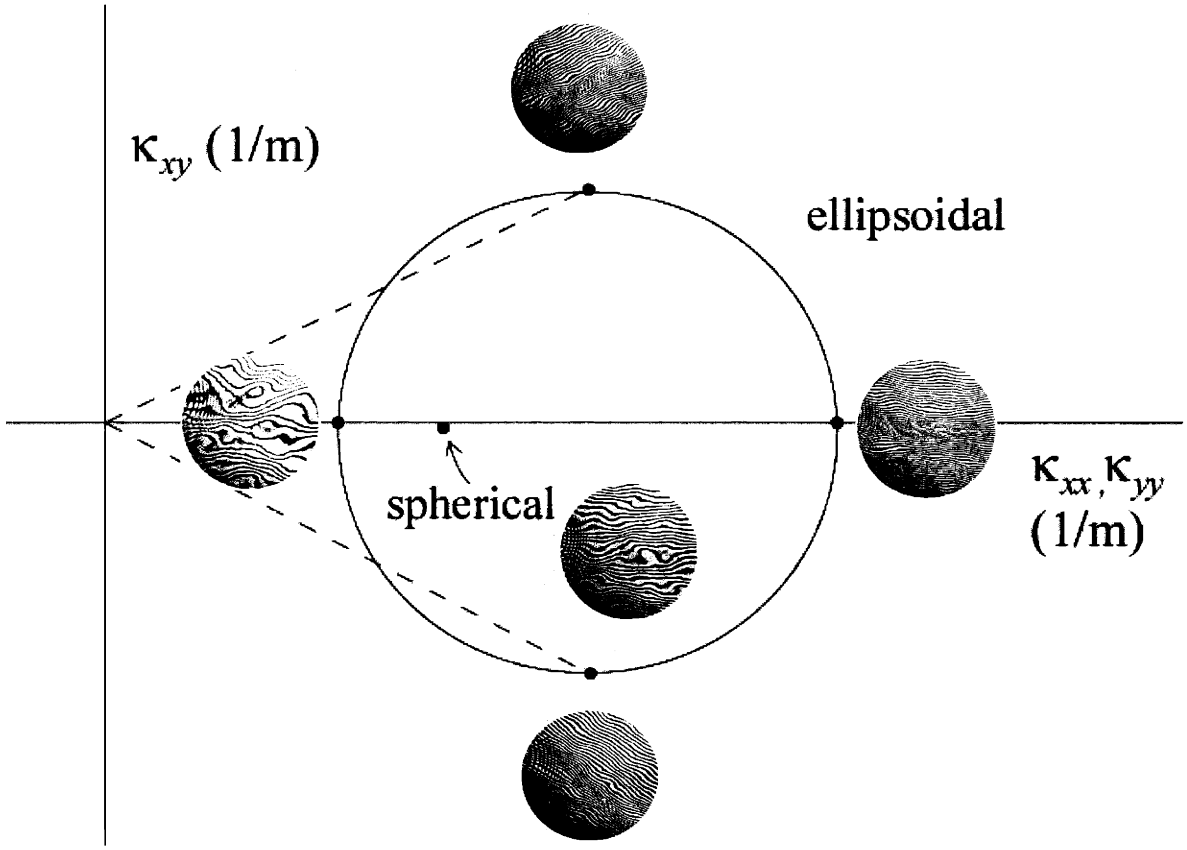

Figure 4-10: A series of images showing the correlation of CGS fringe patterns with points on Mohr's circle for curvatures.

(a)

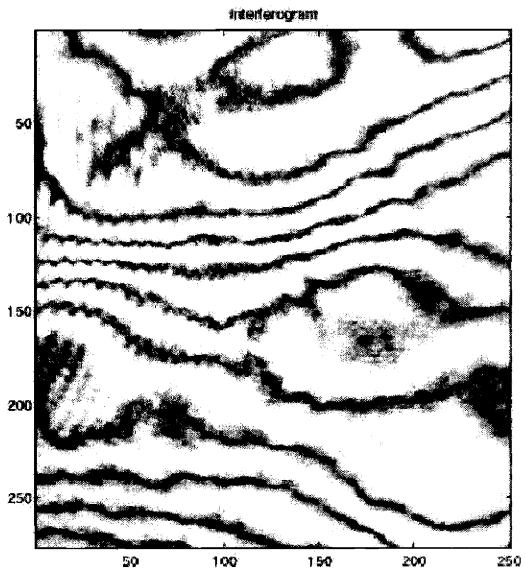

(b)

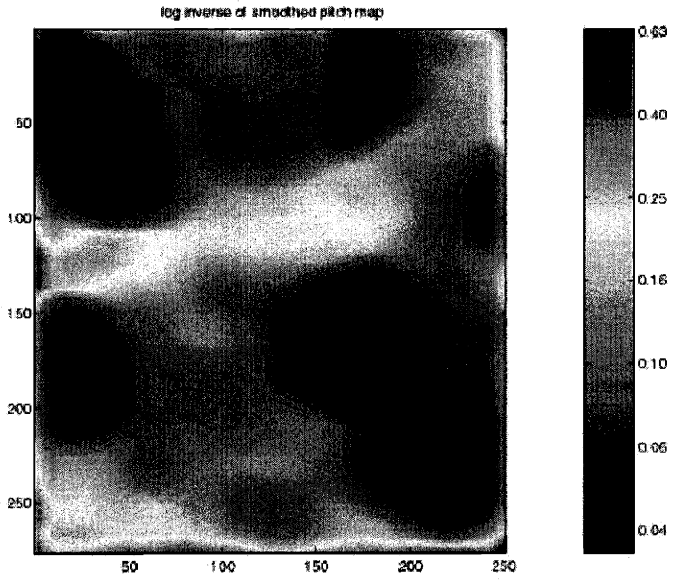

Figure 4-11: Construction of full field curvature map (a) CGS interferrogram of central portion of wafer (0.1mm/point) (b) corresponding full field curvature contour in logarithm scale (the numbers are converted to linear scale in the index)

curvature map in log scale using image processing analysis (b). In Fig. 4-11(a) the pitch (or spacing) between adjacent fringes varies from one region to another. Through the image processing outlined in analysis section, localized curvatures are calculated based on Eq. (4.18). In Fig. 4-11(b), while the region of high fringe density indicates curvature values approximately double the average value ($0.10m^{-1}$), region of low fringe density indicate curvature of less than half this average value. Even in a uniform film, non-uniform curvatures are observed, due to variation of intrinsic and/or processing-induced stresses in the films, as well as large deformation characteristic.

4.5 Conclusions

On the basis of experiments and analyses carried out in the present work for large deformation and bifurcation behavior of W films on Si substrates, the following conclusions are made:

- Coherent gradient sensing (CGS) technique, which is an optical, full field and vibration-insensitive experimental technique, was used to study large deformation behavior by measuring out-of-plane displacement gradient of deformed surfaces in the form of fringes. Since fringe patterns contain information of the wafer surface gradient, curvature can be calculated by taking the derivative of gradient field in the interferogram.

- The measured curvatures in two orthogonal principal directions, the values of which agree reasonably well with both analytical and numerical predictions based on large deformation theory, clearly show that the equilibrium shape of the wafer changes from a sphere to an ellipsoid upon bifurcation.

- In contrast to a one-dimensional scanning method such as laser scanning, which provides only a normal curvature component, twist (shear) as well as normal components of curvatures near the central portion of the wafer can be obtained

as the wafer is rotated with respect to a flat zone. A classical Mohr's circle representation has been used to identify principal directions and rationalize the evolution of twist curvatures for off-principal directions.

- Local curvature variation due to non-uniform film stresses can be captured by a full-field curvature map obtained through numerical differentiation of fringe patterns using image processing analysis.

- The CGS technique can be used for *in situ* quality control of the wafers in semiconductor mass production by monitoring curvature and subsequent stress changes during various fabrication processes such as deposition and thermal cycling.

Chapter 5

Conclusions and Suggested Future Work

The purpose of this thesis is to better understand stresses and deformation of thin films/lines on thicker substrates under internal loadings resulting from material mismatch. As the well-known Stoney formula is limited to isotropic, blanket films that undergo only small deformations, proper interpretation of curvature-stress relationships for new film geometries and for new experimental testing techniques requires an extension of this analytical framework. In particular, this thesis includes an anisotropic modification of the Stoney formula to enable the treatment of periodic line structures such as interconnects on substrates, as well as a large deformation modification of the Stoney formula to enable interpretation of curvature measurements which induce moderate rotation in the film-substrate system. The present work leads to the following conclusions.

- The interconnect structure comprising alternating metal and dielectric lines is characterized by two limiting cases. At low aspect ratios, each metal and dielectric line behaves as an individual thin film, so equibiaxial plane stress conditions prevail in each line. At high aspect ratios, however, the line structure

is homogenized into a single composite layer.

- A simple analytical model based on a composite analogy is used to predict curvature and stress evolution in unpassivated and passivated Cu lines on a substrate in the Damascene process. The effective thermoelastic properties of the composite layer are computed in terms of volume fraction and thermoelastic properties of metal and dielectric lines using standard composite theory. This model enables the calculation of curvature and volume-averaged stress changes during the Damascene process, including polishing and subsequent thermal cycling. In addition, this curvature model can be extended readily to passivated Cu lines, for any passivation material, by superimposing the curvature changes resulting from an additional layer in the regime of linear elasticity.

- Based on the aforementioned analytical solution for volume-averaged thermal stresses in metal and dielectric lines, an engineering map for selection of dielectric materials in integration with Cu metallization is developed. This map indicates low mistmatch stress regime as funtions of modulus and CTE of dielectric materials, which is compatible with Cu interconnect lines as far as thermal stress problem is concerned.

- Three-dimensional FEM results of a bilevel structure indicate that the relative orientation of lines in one level with respect to the other does not significantly affect the individual response of each level. Therefore, it can be seen that interaction between levels in the vertical direction is quite weak when the thickness of the inter-level dielectric (ILD) layer becomes comparable to that of the metal layer.

- The coherent gradient sensing (CGS) technique, an optical, full-field and vibration-insensitive experimental method, are used to study large deformation behavior of thin film-substrate systems by measuring the gradient of out-of-plane displacement of the deformed surfaces. The measured curvatures in two orthogonal principal directions, whose values agree reasonably well with both analytical

and numerical predictions based on large deformation theory, clearly show that the equilibrium shape changes from a sphere to an ellipsoid upon bifurcation.

- The CGS method is used to obtain twist (shear) as well as normal curvature components near the central portion of the wafer as the wafer was rotated with respect to a flat zone. A classical Mohr's circle representation is used to identify principal directions and rationalize evolution of twist curvatures in off principal directions. Local curvature variation due to non-uniform film stresses is captured by full-field curvature map obtained from numerical differentiation of fringe patterns via image processing analysis.

Elastic strain energy stored in lines is released in different forms of inelastic deformation, such as dislocation generation, diffusional creep along grain boundaries in the line or interfaces between the line and the surrounding diffusion-barrier material, and/or fracture-related failure. Therefore, combined analytical and numerical models based on linear elasticity developed in this work can be employed to investigate inelastic behavior in a confined volume with a knowledge of dislocation theory and diffusion kinetics. Furthermore, fracture mechanics approach enables the extension of the current stress modeling to prediction of stress-induced failures, such as cracking, buckling and delamination in the lines on the substrates. The CGS technique and subsequent image processing analysis can be used in monitoring localized curvature variation of wafers during fabrication steps due to its advantages such as real-time, full-field and non-destructive features. Along with detailed finite element analysis, stress distribution in sites vulnerable to failure, *e.g.* edges and corners, can be extracted from the full-field curvature map in a corresponding region, which may enhance productivity and reliability of small volume structure.

Appendix A

Image Processing of CGS Interferograms

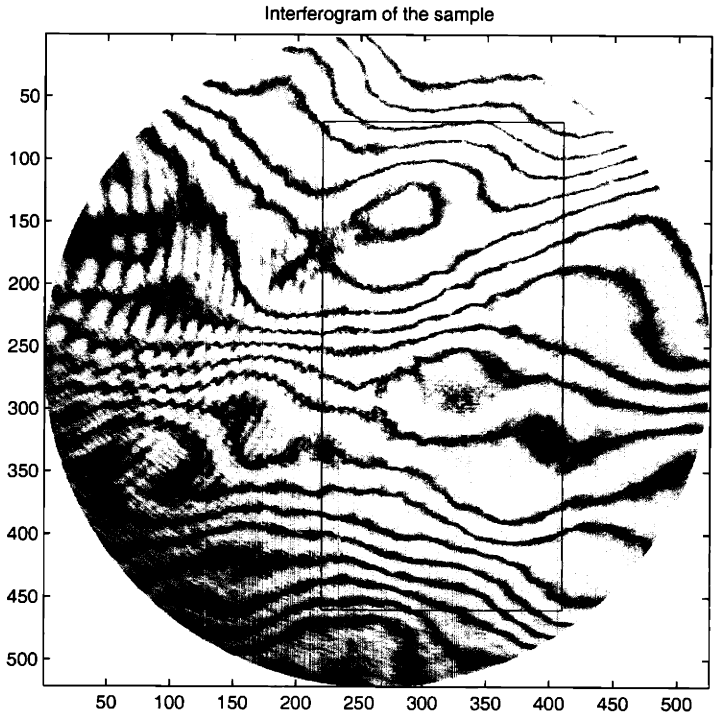

Figure A-1: Original interferogram showing selected region of analysis

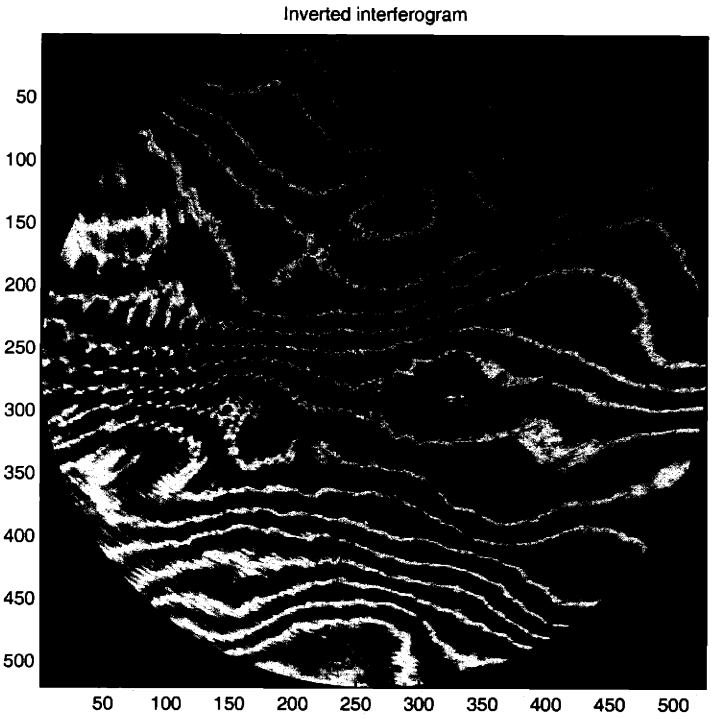

Figure A-2: Inverted image of the original interferogram. Inversion makes valleys of fringes easier to detect.

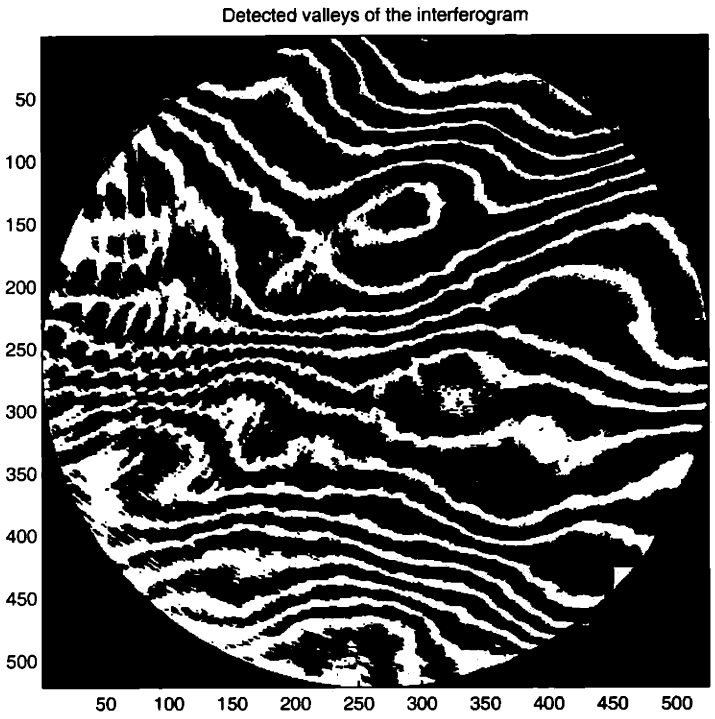

Figure A-3: Detected fringe valleys by thresholding the inverted interferogram.

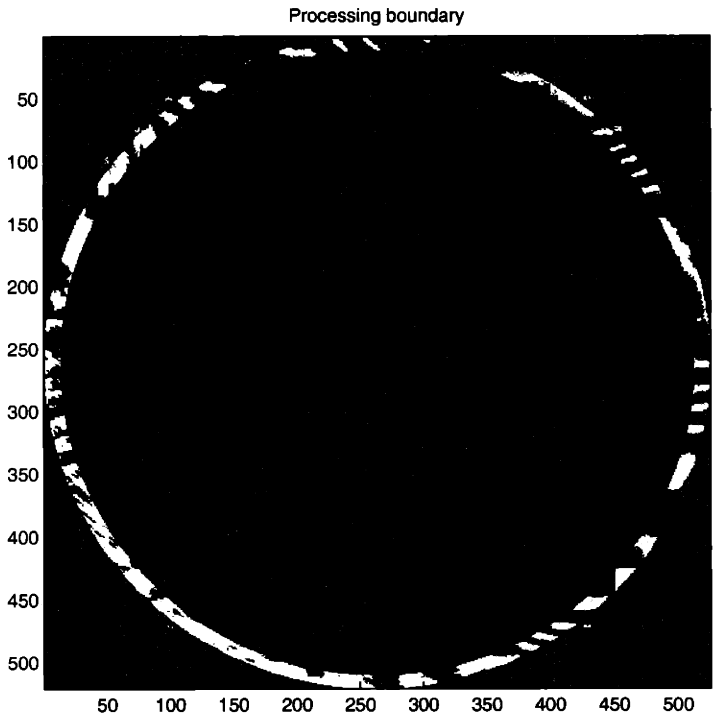

Figure A-4: The same image in Figure A-3 also showing the boundary of the morphological processing. Morphological processing is performed to draw lines with one pixel width along fringe valleys.

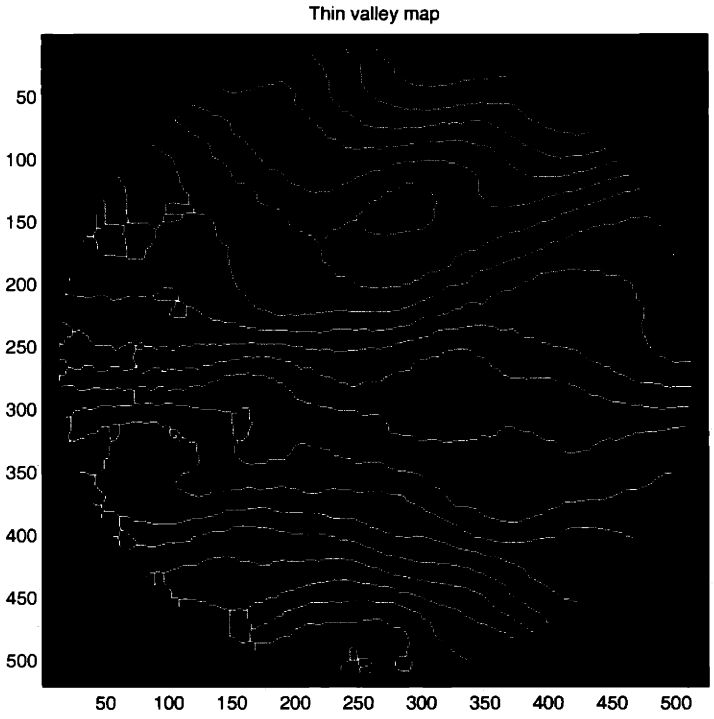

Figure A-5: Result of the morphological processing.

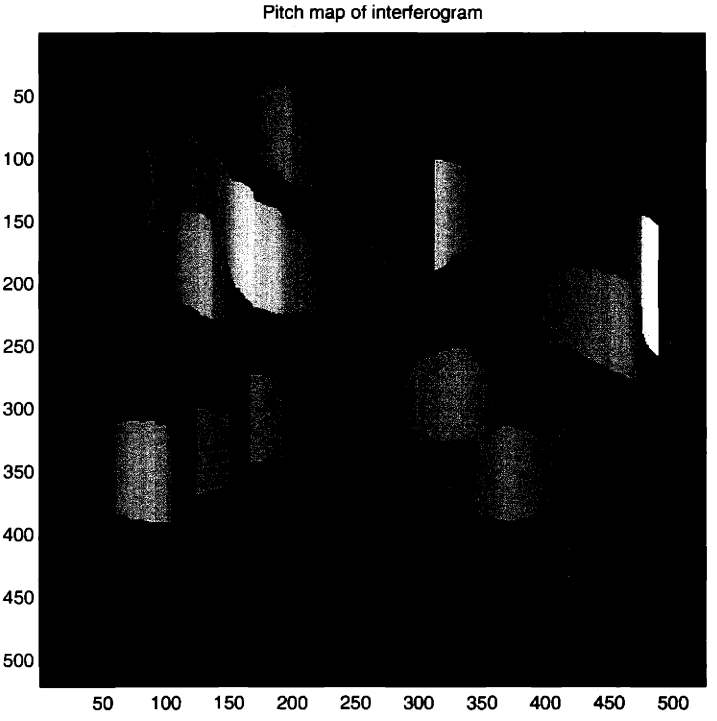

Figure A-6: Pitch (spacing between adjacent fringes) is computed along one direction using Figure A-5 and shown as a gray scale image. In this pitch map, bright color represents long pitch and dark color represents short pitch. Pitch is directed related to the surface curvature.

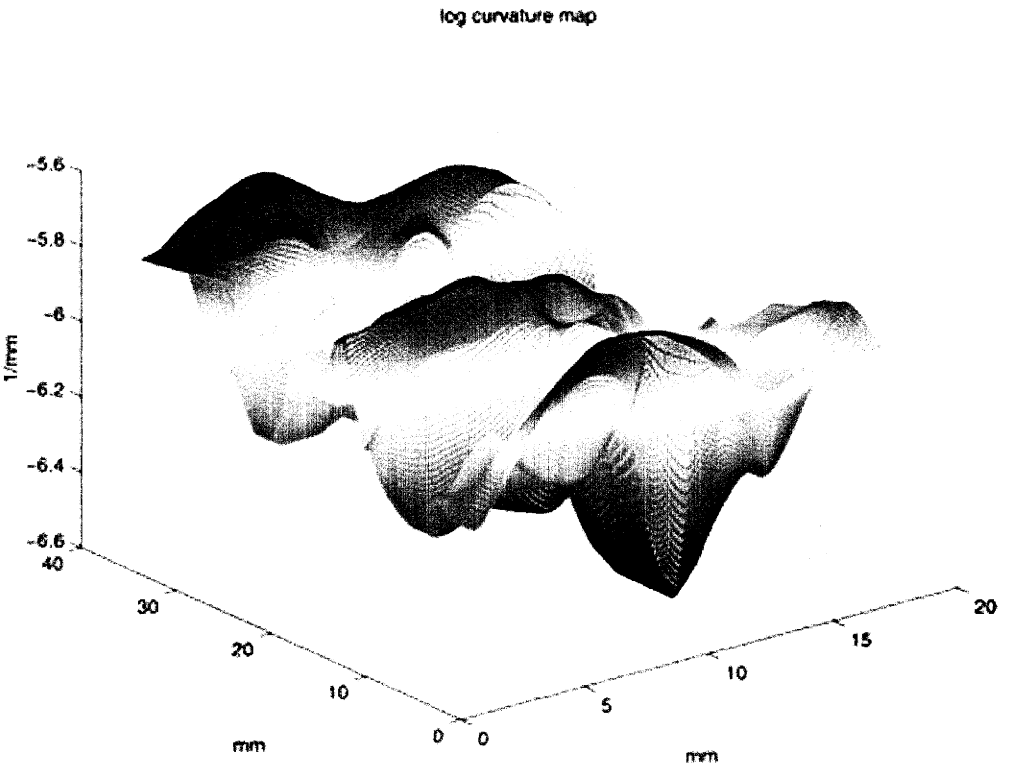

Figure A-7: Curvature map obtained by low pass filtering the pitch map. It is plotted in log scale in units of 1/mm.

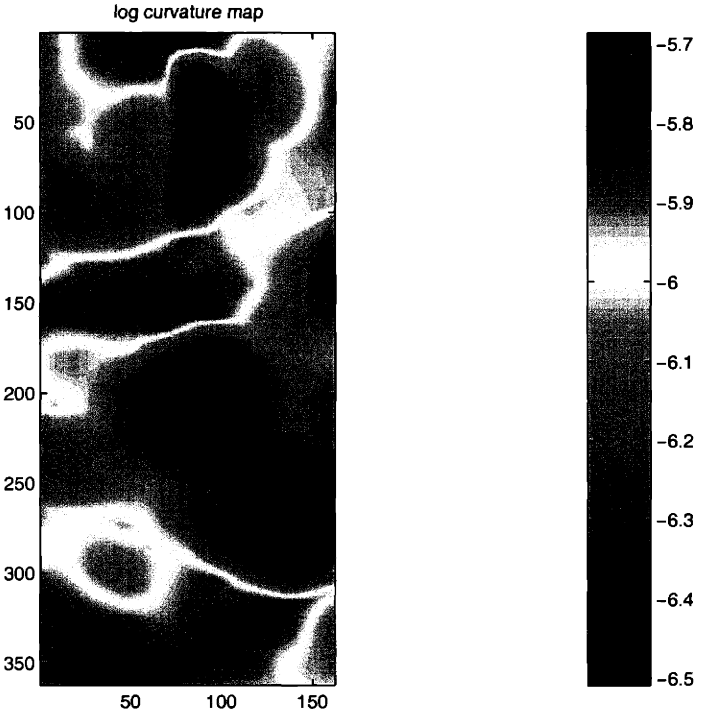

Figure A-8: The same information in Figure A-7 shown as an image.

Bibliography

[1] M. Finot. *Deformation of Multi-layered and Graded Materials: Theory and Experiments.* PhD thesis, Massachusetts Institute of Technology, 1996.

[2] W. D. Nix. *Met. Trans.*, 20A:2217, 1989.

[3] J. L. Beuth. *Int. J. Solids Struct.*, 29:1657, 1992.

[4] J. L. Beuth and N. W. Klingbeil. *J. Mech. Phys. Solids*, 44:1411, 1996.

[5] J. W. Hutchinson and Z. Suo. *Advances in Applied Mechanics*, 29:63, 1992.

[6] J. W. Hutchinson, M. D. Thouless, and E. G. Liniger. *Acta Metall. Mater.*, 40:295, 1992.

[7] M. Y. He, A. G. Evans, and J. W. Hutchinson. *Int. J. Solids Struct.*, 31:3443, 1994.

[8] A. G. Evans and J. W. Hutchinson. *Acta Metall. Mater.*, 43:2507, 1995.

[9] M. Ortiz and G. Gloria. *J. Mech. Phys. Solids*, 42:531, 1994.

[10] A. Bagchi, G. E. Lucas, Z. Suo, and A. G. Evans. *J. Mater. Res.*, 9:1734, 1994.

[11] R. H. Dauskardt, M. Lane, Q. Ma, and N. Krishna. *Engin. Fract. Mech.*, 61:141, 1998.

[12] F. Gaudette, A. E. Giannakopoulos, and S. Suresh. *Int. J. Fract.*, 110:225, 2001.

[13] G. G. Stoney. *Proc. R. Soc. Lond.*, A82:172, 1909.

[14] L. B. Freund and S. Suresh. *Thin Films and Layered Materials: Stress, Deformation and Failure.* Cambridge University Press, Cambridge, U. K., in press.

[15] U. Burges, H. Helneder, H. Kørner, H. Schroeder, and W. Schilling. *Mat. Res. Soc. Symp. Proc.*, 331:247, 1994.

[16] P. H. Townsend, D. M. Barnett, and T. A. Brunner. *J. Appl. Phys.*, 62:4438, 1987.

[17] S. Suresh, A. E. Giannakopoulos, and M. Olsson. *J. Mech. Phys. Solids*, 42:979, 1994.

[18] Y.-L. Shen and S. Suresh. *J. Mater. Res.*, 10:1200, 1995.

[19] P. A. Flinn. *J. Mater. Res.*, 6:1498, 1991.

[20] R. P. Vinci, E. M. Zielinski, and J. C. Bravman. *Thin Solid Films*, 262:142, 1995.

[21] R.-M. Keller, S. P. Baker, and E. Arzt. *J. Mater. Res.*, 13:1307, 1998.

[22] A. Witvrouw, J. Proost, Ph. Roussel, P. Cosemans, and K. Maex. *J. Mater. Res.*, 14:1246, 1999.

[23] S. Suresh, A. Mortensen, and H. McManus, editors. *MIT-ONR Workshop on Functionally Graded Structural Materials*, Cambridge, MA, 1994. Massachusetts Institute of Technology.

[24] L. B. Freund. *J. Cryst. Growth*, 132:341, 1993.

[25] L. B. Freund. *J. Mech. Phys. Solids*, 44:723, 1996.

[26] *The National Technology Roadmap Semiconductor Technology*, 2001.

[27] M. A. Korhonen, P. Børgesen, K. N. Tu, and C.-Y. Li. *J. Appl. Phys.*, 73:3790, 1993.

[28] J. J. Clement and C. V. Thompson. *J. Appl. Phys.*, 78:900, 1995.

[29] R. J. Gleixner, B. M. Clemens, and W. D. Nix. *J. Mater. Res.*, 12:2081, 1997.

[30] B. Greenbaum, A. I. Sauter, P. A. Flinn, and W. D. Nix. *Appl. Phys. Lett.*, 58:1845, 1991.

[31] P. Børgesen, J. K. Lee, R. J. Gleixner, and C.-Y. Li. *Appl. Phys. Lett.*, 60:1706, 1992.

[32] D. Kim, W. D. Nix, M. D. Deal, and J. D. Plummer. *J. Mater. Res.*, 15:1709, 2000.

[33] S. Chiras and D. R. Clarke. *J. Appl. Phys.*, 88:6302, 2000.

[34] T. Marieb, A. S. Mack, N. Cox, D. Gardner, and X. C. Mu. *Mat. Res. Soc. Symp. Proc.*, 403:639, 1996.

[35] M. A. Moske, P. S. Ho, D. J. Mikalsen, J. J. Cuomo, and R. Rosenberg. *J. Appl. Phys.*, 74:1716, 1993.

[36] I.-S. Yeo, S. G. H. Anderson, P. S. Ho, and C. K. Hu. *J. Appl. Phys.*, 78:953, 1995.

[37] M. J. Kobrinsky, C. V. Thompson, and M. E. Gross. *J. Appl. Phys.*, 89:91, 2001.

[38] Y.-L. Shen, S. Suresh, and I. A. Blech. *J. Appl. Phys.*, 80:1388, 1996.

[39] A. Gouldstone, Y.-L. Shen, S. Suresh, and C. V. Thompson. *J. Mater. Res.*, 13:1956, 1998.

[40] A. Saerens, P. Van Houtte, and S. R. Kalidindi. *J. Mater. Res.*, 16:1112, 2001.

[41] H. Niwa, H. Yagi, H. Tsuchikawa, and M. Kato. *J. Appl. Phys.*, 68:328, 1990.

[42] M. A. Korhonen, R. D. Black, and C.-Y. Li. *J. Appl. Phys.*, 69:1748, 1991.

[43] A. Wikström, P. Gudmundson, and S. Suresh. *J. Appl. Phys.*, 86:6088, 1999.

[44] A. Wikström, P. Gudmundson, and S. Suresh. *J. Mech. Phys. Solids*, 47:1113, 1999.

[45] N. Misawa, T. Ohba, and H. Yagi. *MRS Bulletin*, 19(8):63, 1994.

[46] T.-S. Park and S. Suresh. *Acta Mater.*, 48:3169, 2000.

[47] T.-S. Park, M. Dao, S. Suresh, D. Pantuso, and S. Shankar. in preparation.

[48] B. D. Harper and C. P. Wu. *Int. J. Solid Struct.*, 25:511, 1990.

[49] C. B. Masters and N. J. Salamon. *Int. J. Eng. Sci.*, 31:915, 1993.

[50] C. B. Masters and N. J. Salamon. *J. Appl. Mech.*, 61:87, 1994.

[51] N. J. Salamon and C. B. Masters. *Int. J. Solid Struct.*, 32:473, 1995.

[52] M. Finot and S. Suresh. *J. Mech. Phys. Solids*, 44:683, 1996.

[53] M. Finot, I. A. Blech, S. Suresh, and H. Fujimoto. *J. Appl. Phys.*, 81:3457, 1997.

[54] L. B. Freund. *J. Mech. Phys. Solids*, 48:1159, 2000.

[55] A. E. Giannakopoulos, I. A. Blech, and S. Suresh. *Acta Mater.*, 49:3671, 2001.

[56] H. Lee, A. J. Rosakis, and L. B. Freund. *J. Appl. Phys.*, 89:6116, 2001.

[57] T.-S. Park, S. Suresh, J. Ryu, D. M. Freeman, and A. J. Rosakis. in preparation.

[58] C.-K. Hu, B. Luther, F. B. Kaufman, J. Hummel, C. Uzoh, and D. J. Pearson. *Thin Solid Films*, 262:84, 1995.

[59] S. Timoshenko. *Strength of Materials.* Krieger, Huntington, NY, USA, third edition, 1976.

[60] *ABAQUS Version 5.8: General Purpose Finite Element Program.* Hibbit, Karlson and Sorensen Inc., Pawtucket, RI, USA, 1999.

[61] Y.-L. Shen, S. Suresh, M. Y. He, A. Bagchi, O. Kienzle, M. Rühle, and A. G. Evans. *J. Mater. Res.*, 13:1928, 1998.

[62] A. Wikström and P. Gudmundson. *Acta Mater.*, 48:2429, 2000.

[63] *ABAQUS Version 6. 1: general purpose finite element program.* Hibbit, Karlson and Sorensen Inc., Pawtucket, RI, USA, 2000.

[64] S.P Hau-Riege and C. V. Thompson. *J. Mater. Res.*, 15:1797, 2000.

[65] J.-H. Zhao, T. Ryan, P. S. Ho, A. J. McKerrow, and Wei-Yan Shih. *J. Appl. Phys.*, 88:3029, 2000.

[66] Y.-L. Shen. *J. Mater. Res.*, 12:2219, 1997.

[67] M. W. Hyer. *J. Composite Mater.*, 15:175, 1981.

[68] A. J. Rosakis, R. P. Singh, Y. Tsuji, E. Kolawa, and N. R. Moore Jr. *Thin Solid Films*, 42:325, 1998.

[69] *MATLAB Version 6.1: General Purpose Technical Computing Program.* The Mathworks Inc., Natick, MA, USA, 2001.